Blood-Oxygen-Level-Dependent Parameter Identification using Multimodal Neuroimaging and Particle Filters

Aditya Ramesh Mundle

Thesis submitted to the Faculty of the
Virginia Polytechnic Institute and State University
in partial fulfillment of the requirements for the degree of

Master of Science
in
Electrical Engineering

Chris L. Wyatt, Chair
William T. Baumann
A. A. (Louis) Beex

January 19, 2012
Blacksburg, Virginia

Keywords: BOLD Response, Nonlinear Systems, Overparameterization, System Identification, Particle Filter, Multimodal Neuroimaging

Blood-Oxygen-Level-Dependent Parameter Identification using Multimodal Neuroimaging and Particle Filters

Aditya R. Mundle

(ABSTRACT)

The Blood Oxygen Level Dependent (BOLD) signal provides indirect estimates of neural activity. The parameters of this BOLD signal can give information about the pathophysiological state of the brain. Most of the models for the BOLD signal are overparameterized which makes the unique identification of these parameters difficult. In this work, we use information from multiple neuroimaging sources to get better estimates of these parameters instead of relying on the information from the BOLD signal only. The mulitmodal neuroimaging setup consisted of the information from Cerebral Blood Volume (CBV) (VASO-Fluid-Attenuation-Inversion-Recovery (VASO-FLAIR)), and Cerebral Blood Flow (CBF) (from Arterial Spin Labelling (ASL)) in addition to the BOLD signal and the fusion of this information is achieved in a Particle Filter (PF) framework. The trace plots and the correlation coefficients of the parameter estimates from the PF reflect ill-posedness of the BOLD model. The means of the parameter estimates are much closer to the ground truth compared to the estimates obtained using only the BOLD information. These parameter estimates were also found to be more robust to noise and influence of the prior.

Dedicated to my grandparents.

Acknowledgments

First and foremost, I would like to thank my advisor - Dr. Chris Wyatt. I am extremely grateful for his support and patience with me throughout these two and a half years of graduate studies and research. I have learnt more about software engineering during my TA under him in Summer 2011 than my entire college and graduate studies. His work ethic has been a continuing source of inspiration for me.

I don't think I would have been able to cope with the rigors of graduate school had it not been for my first course here - Digital Signal Processing and Filter Design - with Dr. Beex. I have learnt many things in my meetings with Dr. Beex. I would like to thank him for all the advice and support.

I would like to thank Micah for all his help throughout this work. I would like to thank Matt for the discussions about various things (research included), teaching me Cribbage and just being an awesome lab partner!

I have looked up to my parents all my life. Their support, encouragement and guidance in all walks of life has been much more than amazing. I know that they don't really like a formal acknowledgment like this one, but still a big thank you!

To my brother, Abhiram - Your view on life is completely different than mine. I am grateful that you have shown me this other perspective and please be the same always.

Over the past two and a half years, I have made the best friends - Srikrishna, Kaushik, Arijeet, Venkat, Ambooj, Yagnes, Tyagi, Arijita and Danielle. I will not be able to be concise about all the things I need to be thankful for so I would like to just say thanks! Special thanks to Danielle for putting up with me.

Contents

List of Figures

List of Tables

List of Acronyms

AD Alzheimer's Disease 4

ASL Arterial Spin Labelling ii

BOLD Blood Oxygen Level Dependent ii

BPF BOLD Particle Filter 6

CBF Cerebral Blood Flow ii

CBV Cerebral Blood Volume ii

CMRO2 Cerebral Metabolic Rate of Oxygen 12

CSF Cerebrospinal Fluid 20

DTI Diffusion Tensor Imaging 10

EEG Electroencephalography 10

EPI Echo Planar Imaging 3

EKF Extended Kalman Filter 6

fMRI Functional Magnetic Resonance Imaging v

GA Genetic Algorithms 6

GLM General Linear Model 6

GRASE Gradient And Spin Echo 20

Hb Hemoglobin 1

HMM Hidden Markov Models 7

HCT Hematocrit 20

ICP Intra Cranial Pressure 4

KF Kalman Filter 7

MCMC Markov Chain Monte Carlo 15

MCI Mild Cognitive Impairment 4

MEG Magnetoencephalography 10

MRI Magnetic Resonance Imaging 1

MTT Mean Transit Time 12

MPF Multimodal Particle Filter v

NMR Nuclear Magnetic Resonance 1

OEF Oxygen Extraction Fraction 4

PET Positron Emission Tomography 10

PF Particle Filter ii

PCA Principal Component Analysis 19

RF Radio Frequency 1

RBPF Rao-Blackwellized Particle Filter 7

SA Simulated Annealing 6

SIR Sequential Importance Resampling 17

SIS Sequential Importance Sampling 16

TI Inversion Time 20

TR Repetition Time 24

UKF Unscented Kalman Filter 6

VB Variational Bayes 61

VASO Vascular Space Occupancy 20

VASO-FLAIR VASO-Fluid-Attenuation-Inversion-Recovery ii

Chapter 1

Introduction

1.1 fMRI and the BOLD Signal

Magnetic Resonance Imaging (MRI) is used to image the organs - including the central nervous system - and provides information about the physiochemical state of tissues, their vascularization and perfusion [41]. Since the work of [53, 34], it has been possible to get an estimate of neural activity by measuring the hemodynamic changes due to the change in the metabolic state of the brain. This particular method of MRI is known as fMRI.

Nuclear Magnetic Resonance (NMR) is the basic physical phenomenon in MRI. The H_2 atoms of water particles have a property known as spin which makes it behave like a tiny magnet. In a MRI scanner, these spins align with the strong constant magnetic field. When this external field is disturbed, the spin magnetic moments precess at a characteristic frequency ν_0 known as the Larmor Frequency which is dependent on the particular atom (in this case the H_2) and the external field. When a Radio Frequency (RF) pulse is applied orthogonally to the static field at ν_0, there is net magnetization due to the resonance of the atoms at ν_0. This is the radio signal observed from a MRI scanner. After this RF excitation is turned off, the net magnetization returns to the equilibrium state with time.

There are different relaxation times for the longitudinal (static magnetic field) - T1 and the transverse - T2 and T2*. The T2 and T2* are due to the fluctuations in the Larmor frequencies inside the sample (H_2 atoms) at the molecular level (T2) and local inhomogeneities (T2*). T2* is the one responsible for the BOLD contrast. The image intensity is inversely proportional to the inhomogeneities. The BOLD signal is a result of changes in inhomogeneity of the magnetic field within the tissue due to the changes in blood oxygenation. The Hemoglobin (Hb) in the blood is diamagnetic when oxygenated and paramagnetic when deoxygenated. This deoxyhemoglobin distorts the magnetic field in and around the blood vessels creating microscopic inhomogeneous field leading to a change in the local MRI signal. In the event of increased neural activity in the brain, the local CBF increases much more than the CMRO2 which reduces the local oxygen extraction fraction

(E). Thus the local blood is more oxygenated, deoxyhemoglobin content is less and the magnetic field distortions are reduced leading to an increase in the local MRI signal - BOLD [1, 7, 22, 42].

1.2 BOLD Model

The BOLD signal does not measure the neuronal activity directly but is a measure of the changes in CBF , CMRO2 consumption and the CBV which are collectively referred as the hemodynamic response to activation [6, 27, 41]. Understanding the connection between the neuronal activity and the BOLD signal is important for the interpretation and analysis of the fMRI data. The balloon model proposed by [7] describes the link between the CBF (f) and the output BOLD signal (y) through CBV (v) and deoxyhemoglobin content (q) as the state variables. Friston [22] developed a dynamic input-state-output model of the hemodynamic response to the changes in neuronal activity of the form:

$$\dot{X}(t) = f(X(t), u(t), \theta) \tag{1.1a}$$
$$Y(t) = g(X(t), \theta) \tag{1.1b}$$

where f and g are the nonlinear evolution and measurement functions respectively and θ represents the set of model parameters.

This model completed the balloon model [48, 7]. In Friston's extended model, the regional CBF (f) component of the hemodynamic model linearly links the blood flow to the neuronal activity (u) via the synaptic activity (s). With recent modifications to the BOLD output equation [58, 52], the state space model can be written as:

$$\dot{s} = \epsilon u(t) - \frac{s}{\tau_s} - \frac{f-1}{\tau_f} \tag{1.2a}$$
$$\dot{f} = s \tag{1.2b}$$
$$\dot{v} = \frac{1}{\tau_0}(f - v^{\alpha}) \tag{1.2c}$$
$$\dot{q} = \frac{1}{\tau_0}\left(\frac{f(1-(1-E_0)^f)}{E_0} - \frac{q}{v^{1-1/\alpha}}\right) \tag{1.2d}$$
$$y = V_0((k_1+k_2)(1-q) - (k_2+k_3)(1-v)) \tag{1.2e}$$

where

$$
\begin{aligned}
k_1 &= 4.3 \times \nu_0 \times E_0 \times TE = 0.28 \\
k_2 &= \epsilon_0 \times r_0 \times E_0 \times TE = 0.57 \\
k_3 &= \epsilon_0 - 1 = 0.43
\end{aligned}
$$

$\nu_0 = 40.3/s$ is the frequency offset in Hz for fully de-oxygenated blood (1.5T), $r_0 = 25/s$ is the slope relating change in relaxation rate with the change in blood oxygenation Echo Planar Imaging (EPI) sequence, TE$= 40ms$ is the echo time and $\epsilon_0 = 1.43$ is the ratio of signal MRI from intravascular to extravascular at rest. The parameter E_0 is set to 0.4. These are the experimental setup constants [52].

The BOLD model (1.2) takes into account most, but not all of the experimentally observed non-linearities and characteristics of the BOLD response observed. There are more complex models than this BOLD model - models using more parameters than this already overparameterized BOLD model - but their validity has not been established yet [6]. Hence, in this work, we use the Friston's BOLD model. Chapter 5 discusses this aspect in more detail.

1.3 Hemodynamic Parameters

For the model (1.2), there is a total of 7 parameters [22] -

1. **The Neuronal efficacy** (ϵ) reflects the capacity of the stimulus to excite a neuronal response and the efficacy of the resulting synaptic activity to induce the signal and is expressed in terms of event density (number of evoked transients per second). It is proportional to the energy consumption of the cellular activity and is shown to be linearly linked with the mean powers of EEG current sources [71].

2. **The Signal decay time constant** (τ_s) is the time constant which with increasing value will dampen the rCBF response and also suppress the undershoot.

3. **The Autoregulatory feedback time constant** (τ_f) affects the endurance of the BOLD signal when the resonance frequency is decreased.

4. **The Mean transit time constant** (τ_0) is the average time it takes for a cell to pass through the venous compartment which is the resting venous volume (V_0) divided by the resting flow (F_0), V_0/F_0. This governs the speed of the BOLD signal dynamics.

5. **The Stiffness parameter (Grubb's exponent)** (α) [23] describes the non-linear relationship between the CBF and CBV and can be seen as the ratio of normalized CBV to normalized CBF on a log-scale. This relationship can either relate to both the CBF and the CBV being local or localized CBV and globalized CBF. It serves as a measure of the localized CBV changes per unit change of the CBF velocity (CBFV) [37].

6. **The Resting state oxygen extraction fraction** (E_0) defines a baseline level of neuronal activity and is important in determining the nature of evoked fMRI responses. Low values of E_0 indicate areas of increased oxygen consumption and hence increased activity. Regions with low blood flow or tissues with high extraction have higher values of E_0.

7. **The Resting state blood volume fraction** (V_0) is a measure of the voxel occupied by blood at the resting state in a tissue. It can also be thought of as CBV at resting state.

These hemodynamic variables parameterize the BOLD response. They contain important information about the patho-physiological state of the brain and help understand the underlying mechanisms during activity. Understanding brain function in the baseline state is important for understanding normal human performance because it accounts for most of the enormous energy budget of the brain. Such an understanding is also crucial for deciphering the consequences of baseline-state impairment by diseases of the brain such as stroke and Alzheimer's Disease (AD). V_0 (resting state CBV) is an important determinant of Intra Cranial Pressure (ICP) which when increased can lead to ischemic tissue damage and subsequent brain herniation [78]. Increase in τ_0 and decrease in V_0 are a characteristic of the ischemic tissue and can be used to diagnose stroke and chronic carotid occlusive disease [47, 78]. Mild Cognitive Impairment (MCI) is the translational state that goes from normal aging to fully developed dementia and is crucial in identifying individuals at high risk for developing AD [36]. Increased cortical processing and hence neuronal efficacy (ϵ) can be an indication of early stages of AD in patients with MCI [70]. The resting state Oxygen Extraction Fraction (OEF) , E_0, has also been used as a predictor for stroke occurrence in patients with cerebrovascular disease [26]. Increased OEF accompanied by increased CBV is an indication of occluded carotid artery which can lead to ipsilateral stroke [15]. The Grubb's exponent α can be used to study situations with localized cerebral infarction or hemorrhage and provide information about the patho-physiology of the brain [37].

The hemodynamic parameters can be used to predict and diagnose various brain disorders in a non-invasive fashion. Hence it is crucial that we arrive at good estimates of these parameters. Chambers [9] has demonstrated the use of a PF to arrive at the posterior distribution of the hemodynamic parameters of the BOLD model (1.2). Since this BOLD model is underdetermined, the estimates of the parameters exhibit strong correlation which makes it difficult to arrive at a unique estimate. The values of these parameters can be used to draw inferences about the physiological state of the brain and hence it is important to arrive at a single parameter estimate. In this work, we address this issue of parameter identification in a PF framework using multimodal neuroimaging information - CBV form VASO [44, 24], CBF from ASL [18] in addition to the BOLD signal [9].

1.4 Overview

This chapter has introduced the BOLD model and the importance of the hemodynamic parameters. It has also stated the main aim of this work and the approach taken. Alternative methods and

their limitations are discussed in Chapter 2. Chapter 3 describes the CBV and CBF measurement methods. It describes their integration with the BOLD measurement in a PF framework. Chapter 4 describes the various tests used to compare the performance of this method with the method used in [9]. Chapter 5 discusses the results from Chapter 4 and their implications. It also suggests improvements to overcome the limitations of the technique and the future work in this regard.

Chapter 2

Alternate Methods

2.1 Previous Works

Friston et al. [22] was the first work to compute the hemodynamic parameters from fMRI data using voxels selected from regions found to be active by the General Linear Model (GLM) and hence the reliability of this approximation is unknown for regions that are active but avoid detection by conventional tests due to their nonlinearity [9]. Other solutions like Simulated Annealing (SA) and Genetic Algorithms (GA) were found to be extremely time consuming and impractical for actual application [9, 69]. Among Bayesian approaches, the Unscented Kalman Filter (UKF) and the Extended Kalman Filter (EKF) cannot be used because of their Gaussian assumptions and approximations about the nonlinear BOLD model [9]. Johnston et al. [29] used a PF combined with gradient descent algorithm to estimate the parameters and the state variables. The estimates from this work are quite different from most of the other works and the method is also time consuming. Detailed review of these methods can be found in [9].

Chambers [9] used a PF to perform a joint state-parameter estimation of the BOLD model using a BOLD signal as the measurement. In that work, although the BOLD response could be correctly estimated, the parameter estimates exhibited strong correlation which suggested that the BOLD model was underdetermined. The main aim of this work is to confirm this overparameterization of the BOLD model and achieve better identification of these hemodynamic parameters. The PF designed by Chambers [9] is referred to as the BOLD Particle Filter (BPF) and its performance is compared with the method used here.

2.2 Alternate Methods

2.2.1 Parameter Reduction

The high correlation between the parameter estimates from [9] and the sensitivity analysis conclusions [14] suggest that the BOLD model suffers from the ill-posed inverse problem where different values of the parameters can give the same output. Model reduction methods can be used to obtain a lower dimensional model by reducing the number of states with the same output using projection based methods, reduced basis methods, etc. [73, 28, 39]. In parameter reduction, the aim is to reduce the number of unknown parameters by finding out which parameters are unimportant, replacing them by some constant values and then try to estimate the other more important parameters. Even though these methods can give a reduced model describing the same input-output behavior of the nonlinear system, the physical meaning of the parameters is lost. [67] presents a method to identify the parameters whose contribution to the system is marginal and reduce these parameters to obtain a smaller parameter space. Still, the physical meaning of these 'insignificant' parameters is lost. The process of choosing such 'insignificant' parameters will limit the application to special cases where the parameter to be reduced is not important.

2.2.2 Rao-Blackwellization

For a linear Gaussian model, the Kalman Filter (KF) [30] is the optimal solution for the state estimation [72]. Approximate grid-based filters such as the EKF, UKF, Hidden Markov Models (HMM) can be used to approximate the state space when the linear and gaussian assumptions don't hold but they become impractical to implement as the number of dimensions increase [2]. Although the PF provides a trade-off between the accuracy and complexity by using a finite number of particles for approximation, the tradeoff in accuracy can be a problem when the model has high dimensions. For certain nonlinear models (3.5), which have a mixed linear non-linear structure, the state vector can be partitioned such that,

$$x_t = \begin{bmatrix} x_t^l \\ x_t^n \end{bmatrix}, \tag{2.1}$$

where x_t^l denotes the linear state variable vector and x_t^n denotes the state vector with nonlinear dynamics. The linear state variables are then estimated using a KF and the nonlinear state variables are estimated using the PF. This technique is known as Rao-Blackwellization and the filter is called a Rao-Blackwellized Particle Filter (RBPF) [38, 50, 60]. This method is shown to reduce the state and parameter estimates variance when using the same number of particles as in a PF which can help in improving the parameters estimates of the BOLD model (1.2).

BOLD -RBPF implementation

For the BOLD model described by Eq. (1.2), the state variables are $\mathbf{x}_t = [s_t, f_t, v_t, q_t]$. This can be extended to include the parameters, $\theta_t = [\epsilon, \tau_s, \tau_f, \tau_0, \alpha, E_0, V_0]$, resulting in an extended state vector,

$$\mathbf{x}_t = [s_t, f_t, v_t, q_t, \epsilon, \tau_s, \tau_f, \tau_0, \alpha, E_0, V_0]. \tag{2.2}$$

The dynamics of this extended state vector can be modeled by including a noise term which is a Wiener process [58] for fMRI.

$$d\mathbf{x}_t = \mathbf{f}(\mathbf{x}_t, u_t) + \mathbf{G}dw_t, \tag{2.3}$$

where $\mathbf{G}$ is the weighting matrix for the noise process of the states and w_t is a Wiener process. The BOLD output dynamics, y, measured at discrete intervals k are,

$$y_k \quad = \mathbf{h}'\mathbf{x}_k + e_k, \tag{2.4}$$

where $\mathbf{h}'\mathbf{x}$ is the mapping in Eq. (1.2e) and $e_k \sim \mathcal{N}(0, \sigma_e^2)$ is the measurement noise process.

The state vector as shown in Eq. (2.2) can be partitioned into linear/nonlinear parts as shown in Eq. (2.1) where $\mathbf{x}_t^l = [s_t, f_t]$ is the linear state variable vector and $\mathbf{x}_t^n = [v_t, q_t, \epsilon, \tau_s, \tau_f, \tau_0, \alpha, E_0, V_0]$ is comprised of the nonlinear state variables. Using this partitioned state vector, the state space model for this mixed linear/nonlinear hemodynamic model is:

$$\begin{pmatrix} \mathbf{x}_t^l \\ \mathbf{x}_t^n \end{pmatrix} = \begin{pmatrix} \mathbf{A}_t^l & 0 \\ \mathbf{A}_t^n & f^n \end{pmatrix} \begin{pmatrix} \mathbf{x}_t^l \\ \mathbf{x}_t^n \end{pmatrix} + \begin{pmatrix} \mathbf{B}_u^l \\ 0 \end{pmatrix} \mathbf{U}_t + \begin{pmatrix} \mathbf{G}_t^l \\ \mathbf{G}_t^n \end{pmatrix} \mathbf{w}_t, \tag{2.5}$$

$$y_t \quad = h_t(\mathbf{x}_t^n) + e_t. \tag{2.6}$$

f^n are the equations which govern the nonlinear dynamics of the nonlinear state variables,

$$f^n_{9\times 1} = \begin{bmatrix} -\frac{1}{\tau_0} v_t^{1/\alpha} \\ -\frac{q_t}{\tau_0 v_t^{1-1/\alpha}} \\ 0 \\ 0 \\ 0 \\ 0 \\ 0 \\ 0 \\ 0 \end{bmatrix}. \tag{2.7}$$

$\mathbf{A}^n_t$ is the matrix which relates the dynamics of the nonlinear state variables dependent of the linear state variables,

$$A^n_{t\ 9\times 2} = \begin{bmatrix} 0 & -\frac{1}{\tau_0} \\ 0 & -\frac{(1-(1-E_0)^f)}{\tau_0 E_0} \\ 0 & 0 \\ 0 & 0 \\ 0 & 0 \\ 0 & 0 \\ 0 & 0 \\ 0 & 0 \\ 0 & 0 \end{bmatrix}. \tag{2.8}$$

$\mathbf{A}^l_t$ is the matrix which relates the dynamics of the linear state variables dependent of the nonlinear state variables,

$$A^l_{t2\times 2} = \begin{bmatrix} -\frac{1}{\tau_s} & -\frac{1}{\tau_f} \\ 1 & 0 \end{bmatrix}. \tag{2.9}$$

$\mathbf{G}^n_t$ and $\mathbf{G}^l_t$ are the noise weighting matrix for the nonlinear and linear state variables respectively. These are chosen to be $\mathbf{G}^n_t = I_{9\times 9}$ and $\mathbf{G}^l_t = I_{2\times 2}$.

$\mathbf{B}^l_t$ is the input state matrix,

$$B^l_{t2\times 2} = \begin{bmatrix} \epsilon & \frac{1}{\tau_f} \\ 0 & 0 \end{bmatrix}. \tag{2.10}$$

u_t is the input vector for the linear state variables

$$\mathbf{U}_{t2\times 1} = \begin{bmatrix} \mathbf{u}_t \\ 1 \end{bmatrix}, \tag{2.11}$$

and $\mathbf{w}_t$ is the Wiener state noise processes.

Algorithm 1 shows the implementation of RBPF using (2.5) [2, 38, 60].

The BOLD -RBPF implementation, though attractive, suffers from 2 major drawbacks. Significant performance is obtained only when the number of linear states is much greater than the number of nonlinear states [31]. For the BOLD model, out of the 11 states to be estimated, only 2 (s, f) can be marginalized and estimated by KF. Riccatti recursions cannot be used for the BOLD model [60] which can lead to actually increasing the computational complexity of the RBPF and will not give an advantage over using a PF [31, 50].

2.2.3 Using Multimodal Data

Use of multiple sensors for observation can increase the accuracy of the observations and their characterization. They provide complementary information about the underlying physical process, improve the estimation of the unobserved variables and achieve better inferences [25, 45]. Multi-sensor data fusion has been used for enhancing the system capability, performance and reliability in many areas such as target positioning, navigation, and tracking [51, 8], industrial automation [46], remote sensing of weather, natural sources [56], fault detection [64], multimedia analysis [3], biomedical applications [68], etc.

In neuroimaging, multimodal data fusion is of particular importance due to the potential of combining two or more complementary imaging modalities which provide joint inference about the activity, dynamics, and functions by revealing more information than any of the single techniques [21, 4, 59]. Electroencephalography (EEG)-fMRI can be combined to provide higher spatiotemporal resolution and give better constraints solutions for the inverse source localization problem [35, 59]. Magnetoencephalography (MEG)-fMRI, though cannot be obtained simultaneously like EEG-fMRI, can provide better dipole localization for the same inverse problem [5]. MEG-EEG provides superior localization performance to either of the techniques alone [40, 62]. Positron Emission Tomography (PET) can be combined with EEG to study and diagnose pathologies (e.g epilepsy) though the popularity of PET is decreasing because of the need for radioactive tracers and the greater availability of MRI setups. Diffusion Tensor Imaging (DTI) is also being used to validate and enhance the information obtained with other modalities [54, 77, 66]. [5] provides a comprehensive review of the multimodality neuroimaging techniques and various methods of analysis.

Plis et al. [55] has combined MEG and fMRI in a PF framework similar to the method described in this work to improve neural activity tracking. They show some improvement in estimating the

Algorithm 1 RBPF Algorithm

INITIALIZATION

for $i = 1 \dots N_s$ **do**

Set initial weight: $w_0^{(i)}) = \frac{1}{N}$

Draw parameters θ from the prior: $\theta_0^i \sim \alpha(\Theta)$

Set the 4 state priors to steady state values

Compute the initial covariance matrix of $\mathbf{x}^l$: $\mathbf{P}_0^l$

Set the weights: $w_0^i = \frac{1}{N_s}$

Compute initial state estimates: $\hat{\mathbf{x}}_0 = \sum_{i=1}^{N} w_0^{(i)} \mathbf{x}_0^{(i)}$

end for

ITERATION

for $k = 1 : measurements$ **do**

for $i = 1 \dots N_s$ **do**

MEASUREMENT UPDATE

Update importance weights: $w_t^{(i)} = w_{t-1}^{(i)} \mathcal{N}(e, \sigma)$, where $e = y_t - \hat{y}_t$, $\hat{y}_t = h_t(\mathbf{x}_t^n)$

Normalize the importance weights: $w_t^{(i)} = \frac{w_t^{(i)}}{\sum_{i=1}^{N} w_t^{(i)}}$

Update the nonlinear state variables: $\hat{\mathbf{x}}_t = \sum_{i=1}^{N} w_t^{(i)} \mathbf{x}_t^{(i)}$

RESAMPLING

Compute $N_{eff} = \frac{\sum_{i=0}^{N} w_i}{\sum_{i=0}^{N} w_i^2}$

if $N_{eff} < N_R, N_R = min(50, 0.1N_s)$ **then**

Resample

end if

TIME UPDATE

Particle Filter prediction step: $\mathbf{x}_{t+1}^{n,(i)} \sim \mathcal{N}(\mathbf{x}_t^{n,(i)} + \mathbf{A}^n \hat{\mathbf{x}}_{t|t-1}^{l,(i)}, \mathbf{A}^n \mathbf{P}_{t|t-1}^{l,(i)} \mathbf{A}^{nT} + \mathbf{G}^n \mathbf{Q}_t^n (\mathbf{G}^n)^T)$

Kalman Filter time update step for each particle:

$\mathbf{x}_{t+1|t}^{l,(i)} = \bar{\mathbf{A}}^{\mathbf{l}}(\mathbf{x}_{t|t-1}^{l,\hat{(i)}} + K_t(z_t^i - \mathbf{A}^{\mathbf{l}} \mathbf{x}_{t|t-1}^{l,\hat{(i)}})) + \mathbf{B}^l \mathbf{U}_t + \mathbf{G}^l \mathbf{Q}^{ln} (\mathbf{G}^n \mathbf{Q}^n)^{-1} z_t^i$

$\mathbf{P}_{t+1|t}^l = \bar{\mathbf{A}}^l (\mathbf{P}_{t|t-1}^l - K_t \mathbf{A}^n \mathbf{P}_{t|t-1}^l) (\bar{\mathbf{A}}^l)^T$

where,

K_t is the Kalman gain given by, $K_t = \mathbf{P}_{t|t-1}^l (\mathbf{A}^n)^T (\mathbf{A}^n \mathbf{P}_{t|t-1}^l (\bar{\mathbf{A}^n})^T + \mathbf{G}^n \mathbf{Q}_t^n (\mathbf{G}^n)^T)$

$\bar{\mathbf{A}}^l = \mathbf{A}^l - \mathbf{G}^l \mathbf{Q}^{ln} (\mathbf{G}^n \mathbf{Q}^n)^{-1} \mathbf{A}^n$

$z_t^{(i)} = \mathbf{x}_{t+1}^{n,(i)} - \mathbf{x}_t^{n,(i)}$

end for

end for

unobserved states, which are the hemodynamic parameters from the BOLD model, but it is not significant. Adding another source to the BOLD -fMRI signal does not improve the estimation of the under-determined model in this case as this source (MEG) does not provide any additional information about the BOLD model itself. However, this suggests that if additional measurements/observations of the BOLD model are made, there will be a definite improvement in the hemodynamic parameter estimates.

BOLD -fMRI with others

The BOLD signal is a function not only of the changes in CBF , CBV and Cerebral Metabolic Rate of Oxygen (CMRO2) but also the baseline physiological state. This makes it difficult to model the physiological processes in detail [6, 16, 43]. Combining BOLD signal measurements with other measurements which give information about CBF, CBV, and CMRO2 can help to untangle some of the factors influencing the BOLD effect.

One way to approach this problem can be to estimate the value of certain parameters using one or more modalities. These parameters are the fixed values in the BOLD model and then rest of the parameters are estimates in a PF framework.

Perfusion Weighted Imaging (PWI) allows the estimation of CBV and the Mean Transit Time (MTT, τ_0) [47]. These 2 parameters become measured quantities in the BOLD model which enables PWI to be used in conjunction with fMRI to improve the parameter estimates.

For PWI performed using an intravascular contrast agent (e.g Gd-DTPA), the following equations can be obtained using kinetic theory [47]:

$$C_T(t) = \mathrm{CBF}\int_0^t C_a t' R(t-t')dt', \tag{2.12}$$

$$\mathrm{MTT} = \int_0^\infty R(t)dt, \tag{2.13}$$

$$\int_0^\infty C_T(t)dt = p\int_0^\infty C_a(t)dt, \tag{2.14}$$

where C_T is the tissue concentration, CBF (perfusion) is the volume of arterial blood delivered to the tissue per minute per tissue volume, C_a is the arterial tracer concentration, $R(t)$ is the probability that a molecule of tracer that entered the voxel at $t = 0$ is still inside the voxel at a later time t. Mean Transit Time (MTT) (τ_0) is the average time it takes a tracer molecule to pass through the tissue, and p is the blood-tissue coefficient of a tracer.

Eq.(2.12) states that the local tissue concentration C_T at time t equals the sum of all amounts of tracer that entered the voxel at some previous time, weighted by the probability that these amounts are still there at time t, taking into account the imperfect bolus administration through arterial tracer concentration $C_a(t')$. If the tracers remain in the blood, using (2.14) and $p = \mathrm{CBV}$ (for

intact blood-brain barrier),

$$\text{CBV} \quad = \frac{\int_0^\infty C_T(t)dt}{\int_0^\infty C_a(t)dt}. \tag{2.15}$$

In case $C_a(t)$ cannot be measured, relative CBV values can be obtained under the assumption that all the capillaries in the region of interest are fed by the same artery. (The V_0 parameter is CBV measured at resting state [22], [47].)

This approach suffers from some practical limitations. All the direct estimates and relationships are dependent upon the detailed knowledge of $R(t)$ which is not usually available[47]. The other more serious limitation is the use of a intravascular contrast agent for PWI measurements which restricts the participation of subjects and hence the collection of data and the use of complex simulation paradigms [24].

There are other methods which can be used to estimate parameters like E_0 [26], resting state CBV (which is V_0 [63]). But they each give an estimate of just one or two parameters each. Instead of this approach, observations of the state processes will provide better information about the BOLD model and help to decouple the parameters from the composite BOLD signal. Donahue et al. [16] have recently developed a technique which allows the sequential measurement of CBV (v), and CBF (f) with the BOLD response. This work is based on using this procedure to obtain the CBV and CBF measurements and combine them with the BOLD signal as additional observations of the BOLD model and input to the MPF. The next chapter describes this technique in more detail.

Chapter 3

MPF

3.1 Introduction

A multimodal fusion technique aims to improve the state/parameter estimation accuracy of the underlying physical process by incorporating multiple observations. Bayesian methods allow the use of this additional information from multiple data sources better than a deterministic framework [49].

3.2 Mulitmodal Fusion

The complementary information obtained by multiple observations from multiple sources needs to be combined optimally [76]. A probabilistic framework allows information fusion from these multiple sources by using joint probability distributions to encode the conditional dependence structure of its random variables [5]. Consider a model $\mathcal{M}$ with parameters Θ for which we observe data $\mathbf{Y}$. The prior belief in the values of the parameters Θ represents the information about the uncertain parameter Θ and is represented as $p(\Theta|\mathcal{M})$. The posterior distribution of the parameters represents the current knowledge about all these uncertain quantities (including the parameters). Bayes' rule, for the model $\mathcal{M}$, tells how to use the new observation $\mathbf{Y}$ to update the prior and arrive at the updated posterior distribution:

$$p(\Theta|\mathbf{Y},\mathcal{M}) = \frac{p(\mathbf{Y}|\Theta,\mathcal{M})p(\Theta|\mathcal{M})}{p(\mathbf{Y}|\mathcal{M})}, \tag{3.1}$$

where $p(\mathbf{Y}|\Theta,\mathcal{M})$ is the likelihood of the data given the model and the set of parameters. The normalizing constant in the denominator (the evidence) is given as:

$$p(\mathbf{Y}|\mathcal{M}) = \int_{\Theta} p(\mathbf{Y}|\mathcal{M},\Theta)p(\Theta|\mathcal{M})d\Theta, \tag{3.2}$$

which is an integral usually intractable analytically.

Now suppose that the parameter set Θ_1 corresponds to the dataset $\mathbf{Y}_1$, parameter set Θ_2 corresponds to the dataset $\mathbf{Y}_2$ and Θ_{12} is the common parameter set corresponding to $\mathbf{Y}_{12}$ which can be a superset of the $\mathbf{Y}_1$, $\mathbf{Y}_2$ observations. Then, using Bayes' rule (3.1), we can obtain the posterior distributions of the parameters as [75] :

$$\begin{aligned} p(\Theta_1,\Theta_2,\Theta_{12}|\mathbf{Y}_1,\mathbf{Y}_2,\mathbf{Y}_12,\mathcal{M}) \quad \propto \quad & p(\mathbf{Y}_1|\Theta_1,\Theta_{12},\mathcal{M})p(\mathbf{Y}_2|\Theta_2,\Theta_{12},\mathcal{M})p(\mathbf{Y}_{12}|\Theta_1,\Theta_2,\Theta_{12},\mathcal{M}) \\ & p(\Theta_1|\mathcal{M})p(\Theta_2|\mathcal{M})p(\Theta_{12}|\mathcal{M}). \end{aligned} \tag{3.3}$$

In this case, the joint distribution of (3.3) is not of particular importance and hence the marginal distributions of each of the parameters are desired, for e.g.:

$$p(\Theta_{12}|\mathbf{Y}_1,\mathbf{Y}_2,\mathcal{M}) = \int_{\Theta_1}\int_{\Theta_2} p(\Theta_1,\Theta_2,\Theta_{12}|\mathbf{Y}_1,\mathbf{Y}_2,\mathcal{M})d\Theta_1 d\Theta_2. \tag{3.4}$$

For this work, the $\mathbf{Y}_1$, $\mathbf{Y}_2$ and $\mathbf{Y}_{12}$ correspond to v from CBV , f from CBF and y from BOLD output in the BOLD model (1.2) respectively. The parameter set Θ_1, Θ_2 and Θ_{12} correspond to $[\tau_0,\alpha]$, $[\epsilon,\tau_s,\tau_f]$ and $[\tau_0,\alpha,E_0,V_0,\tau_s,\tau_f,\epsilon]$ respectively. To estimate the posterior distribution of the parameters given by (3.3), given the measurements, $\mathbf{Y}_1$, $\mathbf{Y}_2$ and $\mathbf{Y}_{12}$, the PF provides an approximate solution for the analytically intractable integrals in (3.2) and (3.4).

3.3 Particle Filter

3.3.1 General Particle Filter

A PF is a sequential Markov Chain Monte Carlo (MCMC) method used for online parameter estimation when the model is non-linear and/or non-gaussian [2, 49]. In this generalized KF method, the posterior probability density function (pdf) of the state (in this case, the parameters are treated as states yielding a joint state-parameter vector) is constructed on the basis of all the available information and the received measurements. Consider the non-linear system given by (3.5):

$$\begin{aligned} \dot{X} &= f(X,\Theta,w_x), \\ Y &= g(X,\Theta,w_y), \end{aligned}$$

where X is the state vector, Θ is the parameter vector, Y is the measurement and w_x and w_y are the state and measurement noise respectively. Assuming that the system is time invariant and the

input does not directly influence the output, the system can then be written as [9]:

$$\begin{aligned} \dot{X}_k &= f(X_{k-1}, w_x), \\ Y_k &= g(X_k, w_y). \end{aligned} \tag{3.5}$$

A PF aims to evolve the posterior distribution $p(X_k|Y_{0:k})$ which asymptotically approaches the true pdf in two stages: prediction and update. In the prediction stage, the system model is used to predict the pdf forward from one measurement to the next. In this stage, the available pdf at $k-1$, $p(X_{k-1}|Y_{1:k-1})$ is predicted using the Chapman-Kolmogorov equation (under Markovian assumptions) [2]:

$$p(X_k|Y_{1:k-1}) = \int p(X_k|X_{k-1})p(X_{k-1}|Y_{1:k-1})dx_{k-1}. \tag{3.6}$$

In the update stage, at time step k, the latest measurement Y_k is then used to modify the pdf from the prediction stage using Bayes' rule (3.1)

$$p(X_k|Y_{1:k}) = \frac{p(Y_k|X_k)p(X_k|Y_{1:k-1})}{p(Y_k|Y_{1:k-1})}. \tag{3.7}$$

Using (3.6), ()3.7) an optimal Bayes' solution can be obtained [2] but the computation of the posterior density is analytically intractable. The PF uses the **Sequential Importance Sampling!** (**Sequential Importance Sampling!**) algorithm to approximate this intractable posterior density using a finite number of random samples with associated weights, known as particles, to compute estimates. As the number of these particles, N_s approaches infinity, the Sequential Importance Sampling (SIS) approaches the optimal Bayesian estimate - the true posterior density $p(X_k|Y_{1:k})$.

The posterior pdf, $p(X_{0:k}|Y_{1:k})$ is characterized by these particles, $\{X^i_{0:k}, w^i_k\}^{N_s}_{i=1}$ where the support points $\{X^i_{0:k}, i = 0 \dots N_s\}$ have associated weights $\{w^i_k, i = 0 \dots N_s\}$ and $X_{0:k}$ represent the states up to time k. The discrete approximation to the posterior pdf is then given by:

$$p(X_{0:k}|Y_{1:k}) \approx \sum_{i=1}^{N_s} w^i_k \delta(x_{0:k} - x^i_{0:k}). \tag{3.8}$$

The weights w^i_k are computed using Importance Sampling [2] which allows an approximation $\pi(x)$ to the intractable density $p(x)$ such that

$$p(x) \propto \pi(x). \tag{3.9}$$

In the weighted approximation to $p(x)$ given by (3.8), the normalized weight of the i^{th} particle at the k^{th} time is given by

$$w^i \propto \frac{\pi(x^i)}{q(x^i)}. \tag{3.10}$$

The proposal distribution $q(\cdot)$ is called the importance density which is the density of the points. This makes sure that the weight w_k^i depends only on the probability of the particle being correct given all the measurements up to time k and not on the location of the estimation points [9].

Suppose the samples x_k^i are drawn from the importance density $q(\cdot)$, then from (3.9) and (3.10) the weighting is given by

$$w_k^i \propto \frac{p(X_{0:k}^i|Y_{1:k})}{q(X_{0:k}^i|Y_{1:k})}. \tag{3.11}$$

The density $p(X_{1:k}|Y_{1:k})$ is approximated with a new set of samples with the reception of the measurement Y_k at time step k. Using importance sampling, the weights at time step k are given by:

$$w_k^i \propto \frac{p(Y_k|X_k^i)p(X_k^i|X_{k-1}^i)}{q(X_k^i|X_{k-1}^i, Y_k)}. \tag{3.12}$$

For the PF using the Sequential Importance Resampling (SIR) algorithm, the importance density $q(\cdot)$ is the model transition prior [9, 2]:

$$q(X_k^i|X_{k-1}^i, Y_k) = p(X_k^i|X_{k-1}^i). \tag{3.13}$$

Then, from (3.12) and (3.13), the weighting function is given as:

$$w_k^i \propto w_{k-1}^i p(Y_k|X_k^i), \tag{3.14}$$

which can also be written as:

$$w_k^i \propto p(Y_k|X_k^i). \tag{3.15}$$

A particle filter is initialized by drawing the particles from a prior which must be wide enough to explore all the posterior space an converge. This leads to a considerable number of particles developing insignificant weights. Over time, the increasing variance of the importance weights will lead to the degeneracy phenomenon where a large amount of computational effort is devoted to updating particles whose contribution to the posterior pdf is insignificant [2]. Degeneracy can be measured as:

$$N_{eff} \approx \frac{1}{\sum_{i=1}^{N_s}(w_k^i)^2}. \tag{3.16}$$

Instead of the impractical solution of using a very large number particles, resampling can be used to avoid degeneracy. Regularized resampling is one of the resampling techniques which avoids the particle impoverishment problem [9] as well as the degeneracy phenomenon. Thus, particles are then drawn from an approximate posterior to generate a replica of the posterior with better support.

Algorithm 2 Regularized Particle Filter

INITIALIZATION
for $i = 1 \dots N_s$ **do**
  Draw from the prior: $x_0^i \sim \alpha(X)$
  Set the weights: $w_0^i = \dfrac{1}{N_s}$
end for
ITERATION
for $k = 1 : measurements$ **do**
  for $i = 1 \dots N_s$ **do**
    Sample from the importance distribution: $X_k^i \sim q(X_k | X_{k-1}^i)$
    MEASUREMENT UPDATE
    $p(Y_k | X_k^i) = p_e(Y_k - g(X_k^i))$
    $w_k^i = p(Y_k | X_k^i)$
  end for
  Compute N_{eff}
  if $N_{eff} < N_R, N_R = min(50, 0.1N_s)$ **then**
    Resample using a Regularized Resampler
  end if
end for

3.3.2 Multimodal Particle Filter

In the previous section, the equations were derived assuming a single measurement mode. With the availability of multiple measurements, the likelihood corresponding to each mode is considered in the weight assignment to the sample [32]. For the q^{th} measurement mode, $w_k^{i,q}$ denotes the weight of the sample i at the time step k and the measurement is denoted by $Y_k = \{Y_k^q | q = Q\}$ for $q = 1 \dots Q$. Then the weighting function in (3.15) for the q^{th} measurement mode can written as:

$$w_k^{i,q} \propto p(Y_k^q | X_k^i). \tag{3.17}$$

Under the assumption that the measurement processes are independent, the joint likelihood of the measurement modes is the product of the likelihoods of the individual measurement modes $p(Y_k^q | X_{k^i})$ given by:

$$p(Y_k | X_{k^i}) \propto p(Y_k^1 | X_{k^i}) \cdot p(Y_k^2 | X_{k^i}) \dots p(Y_k^Q | X_{k^i}). \tag{3.18}$$

Thus, from (3.17) and (3.18):

$$w_k^i \propto p(Y_k^1 | X_{k^i}) \cdot p(Y_k^2 | X_{k^i}) \dots p(Y_k^Q | X_{k^i}). \tag{3.19}$$

From (3.15) and (3.19), the weight associated with the sample i at time step k for measurement modes $q = 1 \dots Q$ can be written as:

$$w_{k,q}^{i} \propto w_{k}^{i,1} \cdot w_{k}^{i,2} \dots w_{k}^{i,Q}. \tag{3.20}$$

The independence of the measurements can be verified using Principal Component Analysis (PCA) [32]. For this work, the measurements are taken sequentially and hence their independence need not be verified.

Algorithm 3 Multimodal Particle Filter

INITIALIZATION
for $i = 1 \dots N_s$ **do**
  Draw from the prior: $x_0^i \sim \alpha(X)$
  Set the weights: $w_0^i = \dfrac{1}{N_s}$
end for
ITERATION
for $k = 1 : measurements$ **do**
  for $i = 1 \dots N_s$ **do**
    Sample from the importance distribution: $X_k^i \sim q(X_k | X_{k-1}^i)$
    MEASUREMENT UPDATE
    for q=1…Q **do**
      $p(Y_k^q | X_k^i) = p_e(Y_k^q - g^q(X_k^i))$
      $w_k^{i,q} = p(Y_k^q | X_k^i)$
    end for
    $w_k^i = \prod_{q=1}^{Q} w_k^{i,q}$
  end for
  Compute N_{eff}
  if $N_{eff} < N_R, N_R = min(50, 0.1N_s)$ **then**
    Resample using a Regularized Resampler
  end if
end for

3.4 Implementation

3.4.1 Measurement Methods

CBVw fMRI

As noted earlier, using exogenous contrast agents is not feasible for fMRI studies. Instead, the weighting of the CBV and blood oxygen contrasts are varied by measuring the fMRI signals at various inversion times [24]. The Vascular Space Occupancy (VASO) method nulls the intravascular blood signal and the vasodilatory CBV changes can then be inferred from reductions in the detectable tissue signal [16, 43]. Since whole brain coverage with only VASO is not feasible [43], a 3D Gradient And Spin Echo (GRASE) readout appended to the VASO-FLAIR is used to measure a spin-echo signal [16]. The spin-echo signal for an activated (act) or baseline (base) state can be written as:

$$S_{VF}^{j} = (1 - X_{CSF}^{j})(C_{par} - CBV^{j}C_{b})M_{t}e^{-TE\cdot R_{2,t}^{j}}, \tag{3.21}$$

j = activation (act) or baseline (base) state, X_{CSF} is the voxel Cerebrospinal Fluid (CSF) fraction, $C_{par} \approx 0.89$ mL water/mL parenchyma, $C_b \approx 0.87$mL water/blood and $C_{CSF} \approx 1$mL water mL CSF are the parenchyma, microvascular blood (Hematocrit (HCT)$\approx$ 0.37) and the CSF water densities respectively, M_t is the extravascular tissue magnetization, TE is the echo time, $R_{2,t}$ is the transverse relaxation rate of extravascular tissue.

The signal change between the baseline and activation can be written as:

$$\frac{\Delta S_{VF}}{S_{VF}^{base}} = \frac{(1 - X_{CSF}^{act})(C_{par} - CBV^{act}C_{b})}{(1 - X_{CSF}^{base})(C_{par} - CBV^{base}C_{b})}e^{-TE\cdot\Delta R_{2,t}} - 1. \tag{3.22}$$

Solving for CBV_{act} we get,

$$\begin{aligned} CBV^{act} \;=\; & \frac{1}{C_b}\left[C_{par} - \frac{(1 - X_{CSF}^{base})}{(1 - X_{CSF}^{act})}\left(\frac{\Delta S_{VF}}{S_{VF}^{base}} + 1\right)\right] \times \\ & \frac{1}{C_b}\left[(C_{par} - CBV^{base}\cdot C_b)e^{TE\cdot\Delta R_{2,t}}\right]. \end{aligned} \tag{3.23}$$

CBFw MRI

A CBFw image is generated by subtracting a magnetically tagged (using RF pulse) image from a control image (no blood water tagged). Similar to the 'only VASO' method above, it is not possible to acquire a whole brain image due to the timing discrepancy in the blood water Inversion Time (TI) [16, 43]. To overcome this, a 3D GRASE readout follows the ASL measurements to acquire the entire brain which is also superior to the 2D EPI acquisition.

The CBF can be computed on a per pixel basis as [18]:

$$CBF = \frac{\Delta M}{M_0} \frac{\lambda}{2\alpha} \frac{R_{1a}}{exp(-wR_{1a}) - exp(-(\tau + w)R_{1a})}. \tag{3.24}$$

ΔM is the signal difference between label and control images, M_0 is the control image density, $\lambda = 0.9$mL/ g is the blood/tissue water partition coefficient, $R_{1a} = 0.67s^{-1}$ is the longitudinal relaxation rate of blood, $\tau = 2s$ is the duration of the labeling pulse, $w = 1.2s$ is the post-labeling delay and $\alpha = 68\%$ is the labeling efficiency.

3.4.2 Model

The CBV and the CBF measurements, along with aBOLD measurement, can be acquired sequentially using gradient-echo BOLD EPI, 3D GRASE ASL and 3D GRASE VASO-FLAIR [16, 43]. The CBV and CBF measurements are the v and f state variables in the BOLD model which become the observations in addition to the BOLD measurement.

For the non-linear BOLD model of the form (3.5) given by (1.2), the state vector is $X = [s, f, v, q]$. For the MPF, the state vector is extended to include the parameters $\Theta = [\tau_0, \alpha, E_0, V_0, \tau_s, \tau_f, \epsilon]$ [9], thus the state vector is then given as $X = [s, f, v, q, \tau_0, \alpha, E_0, V_0, \tau_s, \tau_f, \epsilon]$. The actual measurements now are $BOLD : Y^1 = Y^{BOLD}; CBVw : Y^2 = Y^{CBV}; CBFw : Y^3 = Y^{CBF}$ and the measurement estimates for the MPF for each of the three measurements are y, v, f given by (1.2e, 1.2c, 1.2b) respectively. The weighting function update in the measurement stage of (3), for $Q = 3$, can then be written as:

Algorithm 4 Weighting function update

for $k = 1 : measurements$ **do**
  for $i = 1 \dots N_s$ **do**
    $p(Y_k^1|X_k^i) = p_e(Y_k^{BOLD} - y)$
    $p(Y_k^2|X_k^i) = p_e(Y_k^{CBV} - v)$
    $p(Y_k^3|X_k^i) = p_e(Y_k^{CBF} - f)$
    $w_k^i = p_e(Y_k^{BOLD} - y) \cdot p_e(Y_k^{CBV} - v) \cdot p_e(Y_k^{CBF} - f)$
  end for
end for

3.4.3 Particle Filter Settings

Most of the design choices for the MPF were similar to the BPF designed by Chambers [9]. This also demonstrates the extensibility advantage of a Bayesian method like PF.

Table 3.1: The distribution of the priors here is Gamma (Γ) which takes into account the biophysical fact that these values can never be negative. The only change from [9] has been highlighted in red. The location (k) used in [9] was 0.98 which was modified slightly for this work to 1.18 as it achieved optimal estimates. Interestingly, this is the value estimated by [69] for the τ_0 parameter.

Parameter	Definition	Distribution
τ_0	Mean transit time	$\Gamma(1.18, 0.25)$
α	Stiffness parameter	$\Gamma(0.33, 0.045)$
E_0	Resting state O_2 fraction	$\Gamma(0.34, 0.03)$
V_0	Resting state CBV	$\Gamma(0.04, 0.03)$
τ_s	Signal decay time constant	$\Gamma(1.54, 0.25)$
τ_f	Autoregulatory feedback time constant	$\Gamma(2.46, 0.25)$
ϵ	Neuronal efficacy	$\Gamma(0.7, 0.6)$

Prior Distribution

Priors heavily influence the final estimates for a MCMC method like PF [2]. A very wide prior may not converge unless sufficiently large numbers of particles is used and a narrow prior may miss the true value by introducing a bias. Initially, the priors from [9] were used which have been manually tuned for that BPF. Those priors work for all but the τ_0 parameter. In initial tests, this parameter did not converge. After further testing, the value of the prior which gives the optimal solution was found to be slightly different than the one in [9]. These values are tabulated in Table 3.1

Number of Particles: N_s

The density of the posterior distribution approximation is directly proportional to the number of particles (N_s) used but the computational complexity also increases with the N_s. On the other hand, insufficient N_s will give inconsistent estimates. Choosing N_s is more of a trial and error process. For this work, N_s was set to 1000 as described in [9] to be minimum for consistent results. Since the MPF makes use of more information to arrive at the posterior distribution, the effect of fewer than 1000 particles was explored and compared with the estimates for BPF.

Resampling

Resampling improves the performance of a PF [2]. A Gaussian kernel for regularized resampling was chosen since it is simple to sample from and long tailed [9]. Resampling occurs when the N_{eff} drops below the N_R threshold (which is 50 for 1000 particles).

Weighting Function

The distribution of the importance density $p(Y_k|X_k)$, which is set as the error between the estimated and the actual measurement, is chosen as Gaussian. As noted in [9], using Laplacian or Cauchy instead of Gaussian leads to heavy tails which does not penalize the particles in the wrong place as much and leads to a slower convergence. The scale (σ) of this importance density, $\mathcal{N}(Y^q - g^q(X), \sigma)$, has a big influence on the MPF convergence. A big scale will lead to a slow convergence while a narrow scale will lead to particle deprivation. The σ value of 0.005 used in [9] will be very strict in penalizing errors and lead to particle deprivation since the net weighting function is a product of 3 other weighting functions - each from BOLD, CBF and CBV measurements. After trial and error, the scale with optimal performance was found to be 0.1.

Chapter 4

Experiments and Results

4.1 Setup

A single voxel was simulated using the BOLD , CBV and CBF equations from (1.2). This single voxel was realized under different conditions as described in Sections 4.2-4.5. These tests were used to compare the parameter estimation performance of the BPF - the PF used by [9] and the MPF designed in this work. The stimulus to the model is a block-design generated by convolving a 0.5s rect-pulse with a random stimulus generated from a binomial distribution. The default length of the stimulus was 600s as it is sufficient for the BOLD response estimate to converge [9]. The Repetition Time (TR) for the BOLD , CBV and CBF was set to 2.1s, thus giving 256 measurement points as input to the BPF and MPF. The following sections show the parameter estimation performance of the BPF vs MPF plotted as boxplots. The parameter values (true) used to generate the voxels and measure the performance are shown in Table 4.6.

Table 4.1: Ground truth values of the parameters used for the simulation of the BOLD , CBV and CBF voxels for sections 4.2, 4.3, 4.5.

Parameter	Value
τ_0	1.45
α	0.3
E_0	0.47
V_0	0.044
τ_s	1.94
τ_f	1.99
ϵ	1.8

4.1.1 Box-Plots

A boxplot (or a box-whisker plot) summarizes a batch of data by displaying its main features which contain information about the location and spread of the univariate data [19]. The rectangular box's (Fig. 4.1) upper and lower ends refer to the 1^{st} (Q_1) and the 3^{rd} (Q_3) quartile of the data - the 25^{th} and the 75^{th} percentile. A line near the middle of this box is the median - the 50^{th} percentile. The whiskers of the box represent the lowest datum within the $1.5 \times Q_1$ and the highest datum within $1.5 \times Q_3$ among other possibilities [19] and can be called outliers. These are represented by a plus sign in red in the plot. In this chapter the parameter estimate results are plotted as the mean values of a parameter estimate for 25 trial runs of 1 test (e.g. τ_0 estimate obtained using MPF for all pure measurements, $N_s = 1000$, $\sigma_{wf} = 0.1$) are plotted as boxplots and compared to the estimates of the same parameter obtained in one or more different tests. Multiple runs, in this case 25, of 1 test were done to mitigate the random errors in estimation as the draw from the priors is random which might lead to a different posterior distribution and sometimes completely different estimates.

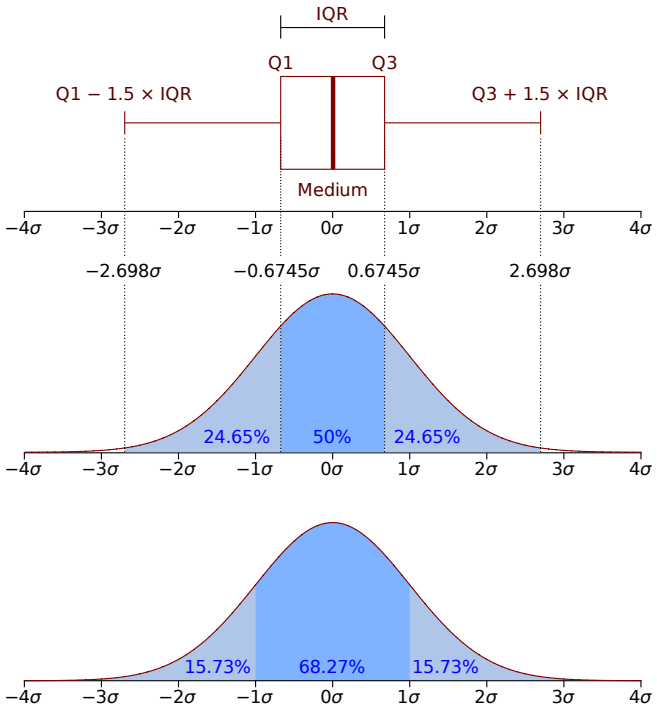

Figure 4.1: Boxplot and its graphical comparison with a gaussian probability distribution $\sim \mathcal{N}(0, \sigma^2)$.

4.2 Pure Signal

The BOLD , CBV and CBF forward models were used to generate 3 voxels (Fig. 4.2-4.4) with no additive noise using the block-design input stimulus. The BPF takes only the BOLD voxel as the measurement whereas the MPF uses all 3 - BOLD , CBV and CBF - as the measurements.

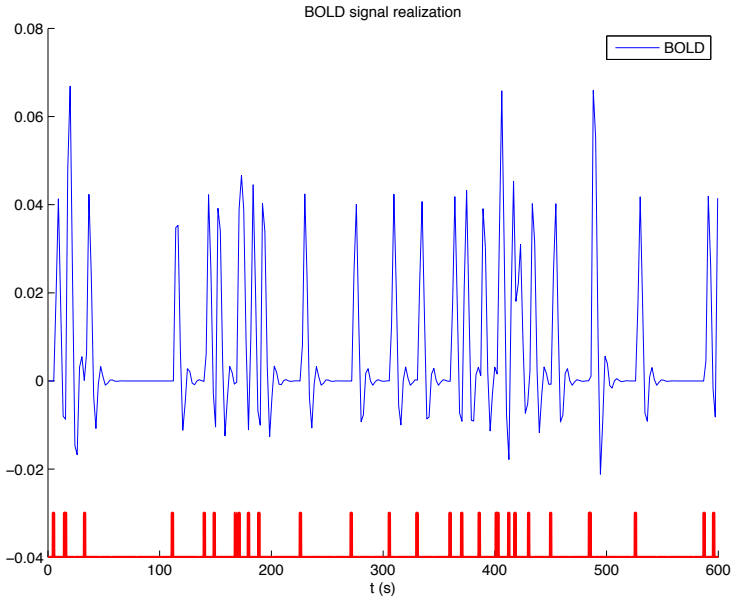

Figure 4.2: BOLD signal realization for a single voxel for a 600s long, block-stimulus (0.5s duration) input (shown at the bottom of the plot). Note that it starts from a steady state value of 0.

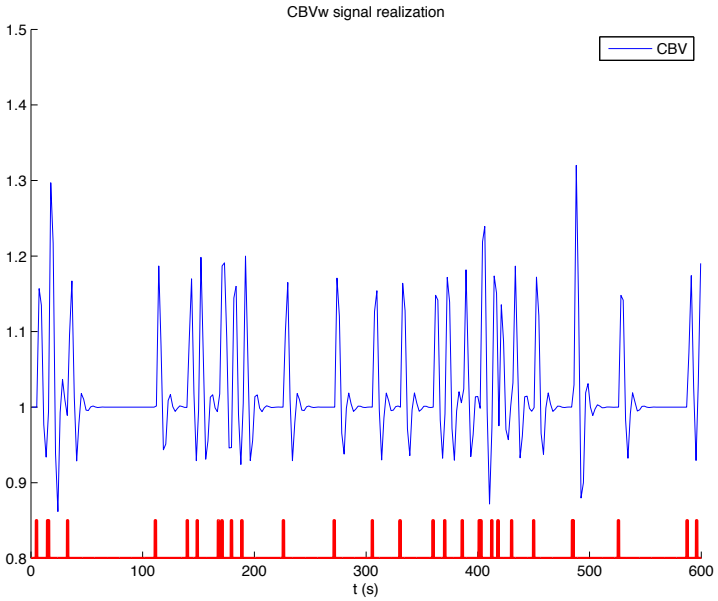

Figure 4.3: CBVw signal realization for a single voxel for a 600s long, block-stimulus (0.5s duration) input (shown at the bottom of the plot). It starts from a steady state value of 1.

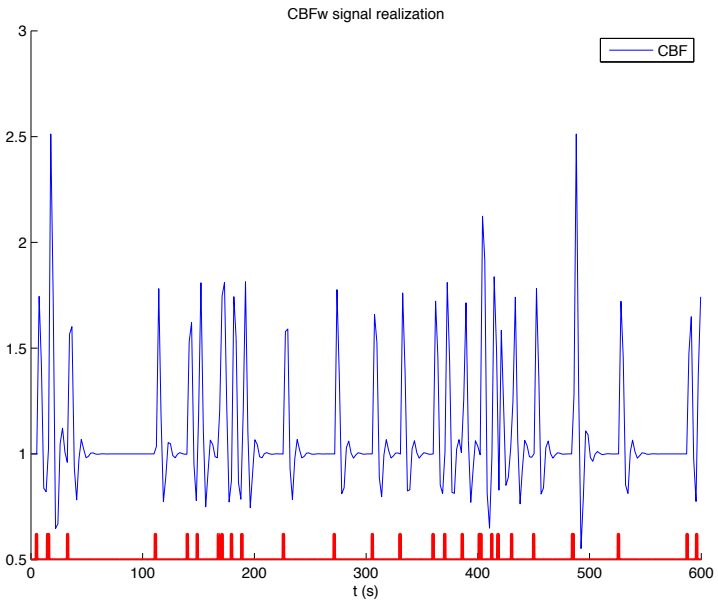

Figure 4.4: CBF w signal realization for a single voxel for a 600s long, block-stimulus (0.5s duration) input (shown at the bottom of the plot). It starts from a steady state value of 1.

4.2.1 Parameter Estimates

From the boxplots (Fig. 4.5-4.11) it can be seen that the parameter estimates obtained using the MPF have significantly improved for most parameters (all except τ_0 and E_0). The BOLD output y for the MPF is now corrected with the modified weighting function which reduces the error in estimation by 50%. Even though there are no parameters associated with CBF (f) directly, f is a function of ϵ, τ_s, τ_f through s. The direct measurement of the CBF and hence f results in the mean being closer to the ground truth - mean errors for these 3 parameters are $\approx 2\%$. The variance of the estimates has also reduced for these three parameters. Error in α estimates is down to 3% due to its relationship with v which is measured directly as CBV. τ_0 estimates obtained using the MPF do not show an improvement over the BPF ones. E_0 estimates do not show any significant change which is expected since none of the new measurements, or the old measurement, have direct information about it. Table 4.2 below shows the ($\%$) error of the mean of the estimates from the BPF and MPF.

Table 4.2: Percentage error in parameter estimates (mean) averaged over 25 runs of no-noise BOLD , CBV w and CBF w measurements using BPF and MPF. Major improvements can be seen in most of the parameter estimates with τ_s,τ_f, and ϵ being the most notable.

	τ_0	α	E_0	V_0	τ_s	τ_f	ϵ
BPF	15.29	14.11	28.24	76.8	10.72	9.697	28.52
MPF	18.62	3.527	27.66	24.85	2.075	1.595	1.348

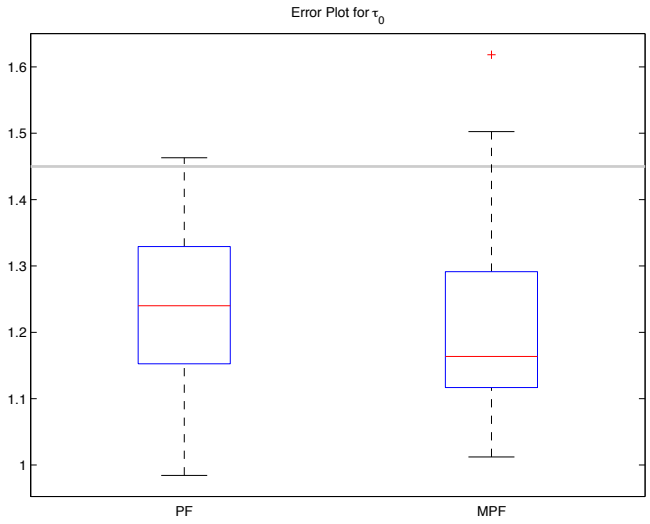

Figure 4.5: τ_0 estimate for pure measurement: There is no marked improvement in the MPF estimates for this parameter.

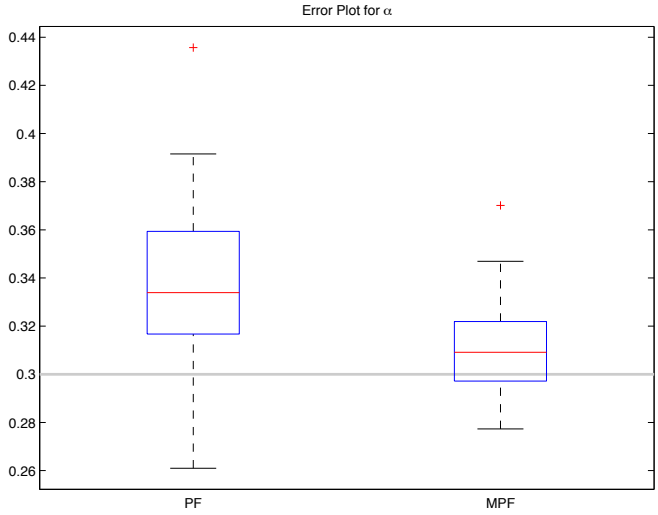

Figure 4.6: α estimate for pure measurement: The variance has reduced as well as the median of the estimates has stayed closer to the ground truth for the MPF estimates.The BPF error was 14.11% which was reduced to 3.57% when estimated by the MPF.

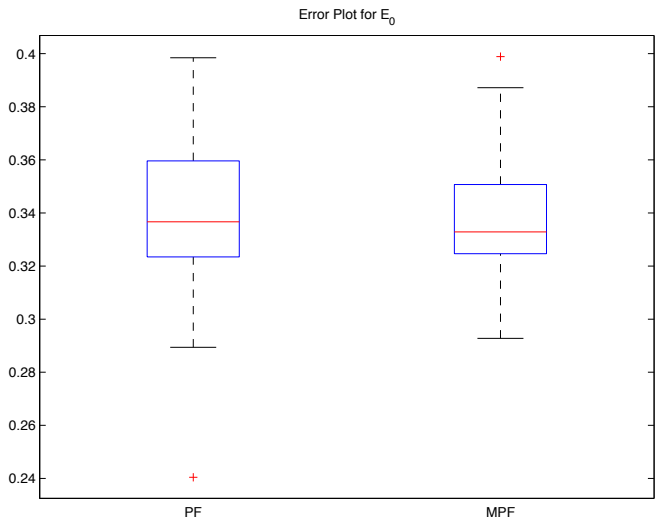

Figure 4.7: E_0 estimate for pure measurement: There is no considerable improvement in the estimates since there is no new information about this parameter in the new measurements. Even though the MPF estimate has marginally smaller variance, it is due to the random nature of the PF estimation (filtering process).

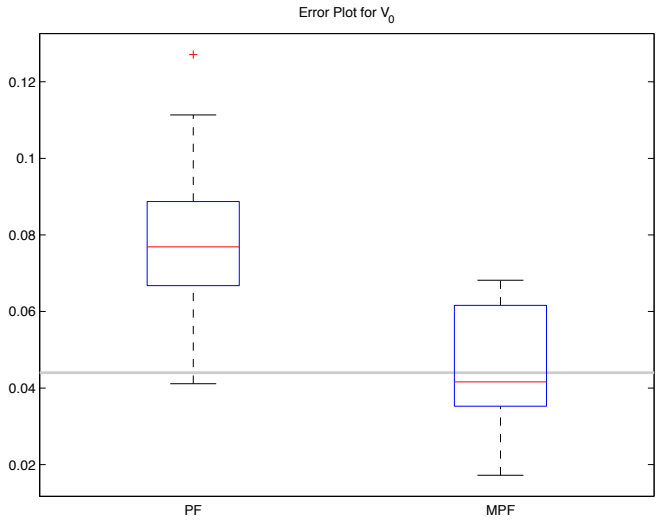

Figure 4.8: V_0 estimate for pure measurement: The median of the mean of the estimates is around the true value for the MPF estimates. The $\%$ error of the estimates reduced to 24.85% for the MPF from a high 76.8% for the BPF.

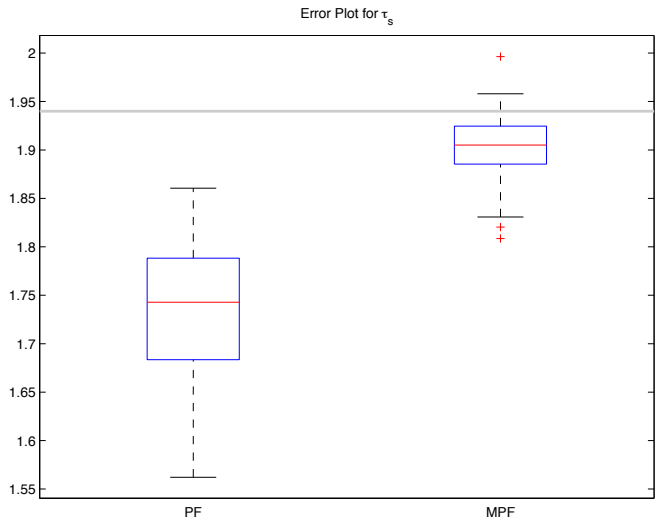

Figure 4.9: τ_s estimate for pure measurement: The MPF estimates are much closer to the actual value with the avg. $(\%)$ error being 2.075% compared to $10.72\%)$ for the BPF. The variance has also reduced which indicates that there were far less random errors in estimation.

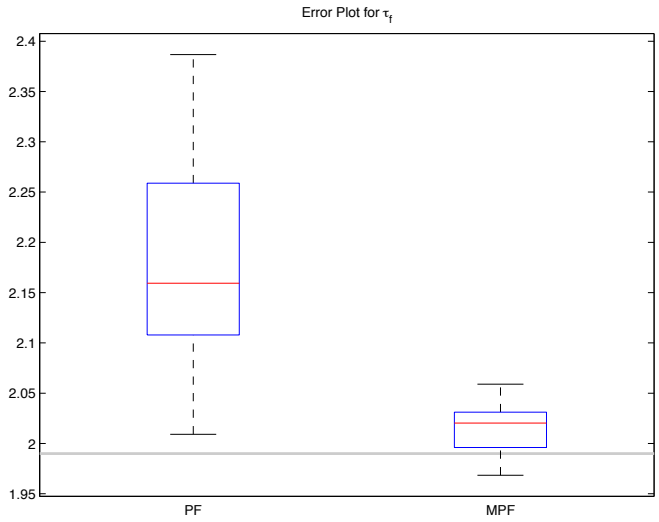

Figure 4.10: τ_f estimate for pure measurement: The MPF estimates have much better mean - error 1.595% for the MPF against 9.697% for the BPF estimates. Again, the variance for the MPF estimates has sharply decreased.

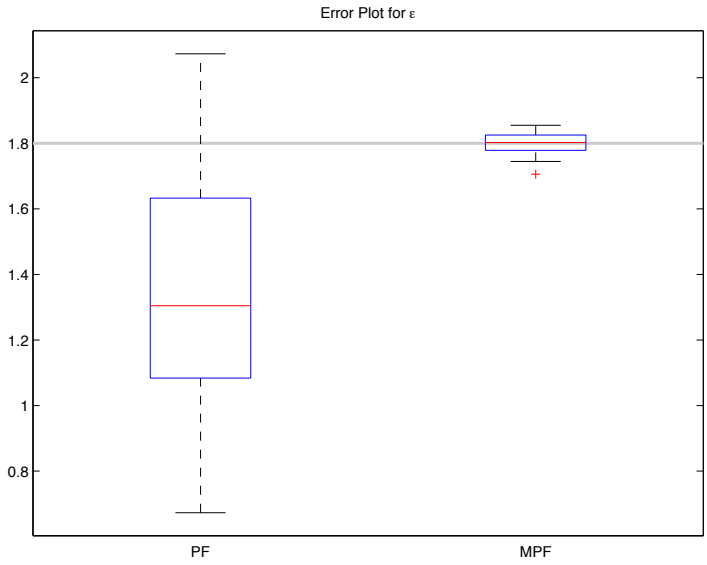

Figure 4.11: ϵ estimate for pure measurement: The mean value from the MPF estimates is just 1.348% whereas the BPF had an error of 28.52% during estimation. This variance for the MPF estimates is very narrow and around the true value.

4.2.2 Convergence

For a MCMC method like PF, the parameter estimates should converge to a steady state value to conclude that they have reached the true value. Trace plots of the estimates during a filtering run can be examined to check if the estimates have converged. If the trace plots show trending i.e slow moving towards some particular value, then the estimates have probably not converged. On the other hand, if the estimates have converged, the trace plots look like a snake around particular value but not moving to another. The BPF estimates trace plots show this kind of trending which is due to the slow convergence of the parameter estimates. On the other hand, the MPF estimates reach a steady state earlier which suggests that the estimates have converged using the additional measurements (Figs.4.12-4.18).

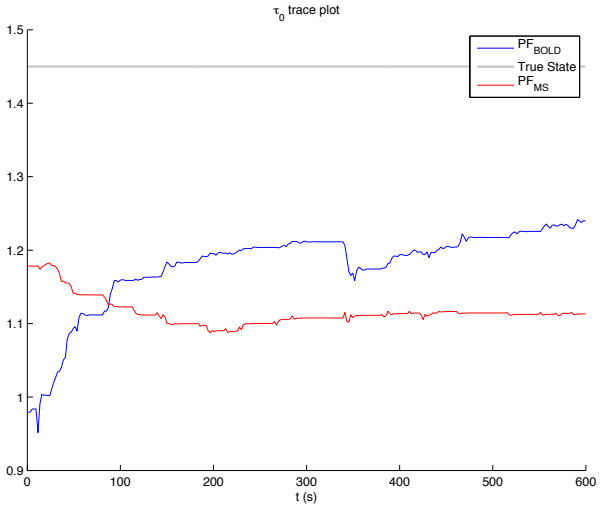

Figure 4.12: τ_0 estimate trace plot: The MPF converges quite early ($\sim$250s). The BPF keeps trending till the end of the measurement, suggesting non-convergence.

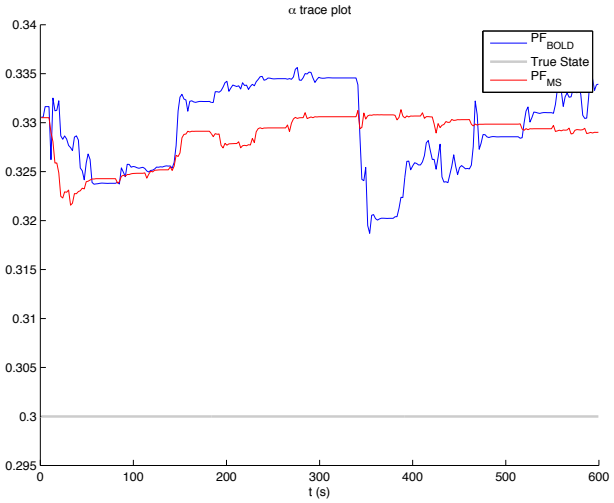

Figure 4.13: α estimate trace plot: The MPF converges to a steady state at $\sim$300s. The BPF estimate, however, does not converge.

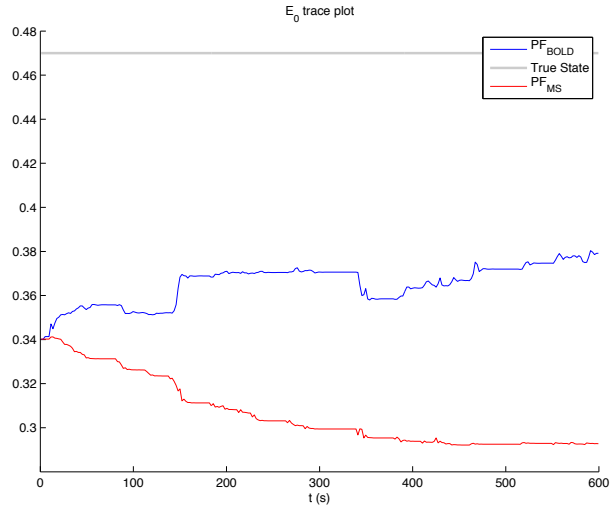

Figure 4.14: E_0 estimate trace plot: The MPF estimate converges to a steady state at $\sim$350s while the BPF estimate does not converge. Even though both are away from the ground truth, the trending of the BPF trace towards the true value does not guarantee that it will actually converge to that value.

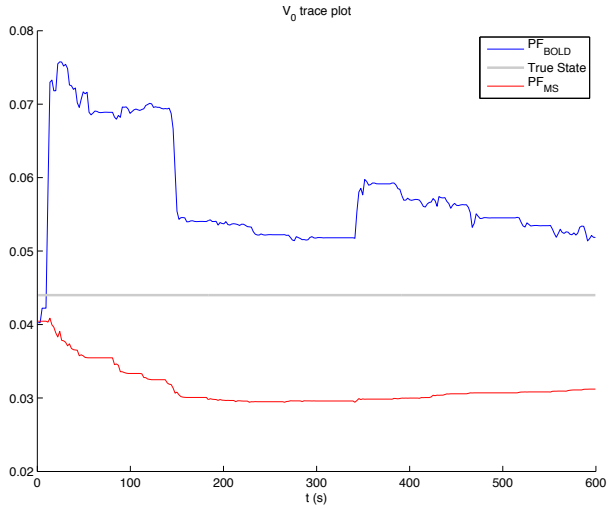

Figure 4.15: V_0 estimate trace plot: The MPF reaches a steady state quite early in the measurement process ($\sim$ 150s) whereas the BPF is still searching i.e. non convergent.

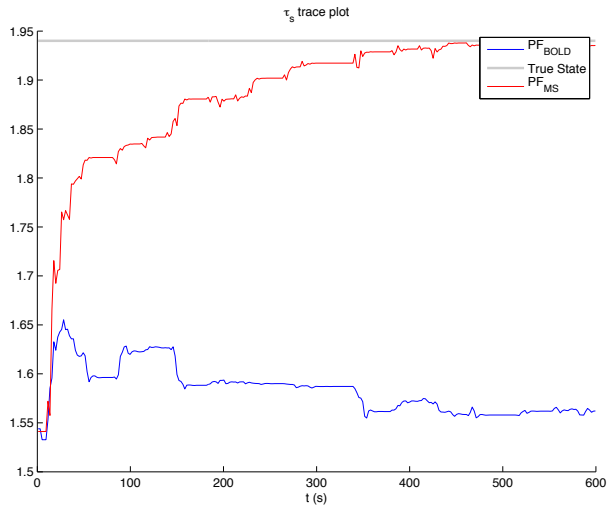

Figure 4.16: τ_s estimate trace plot: The MPF reaches the true value quickly even though it starts quite far from it. The BPF does converge, but towards the end of the measurement process and much further away from the ground truth.

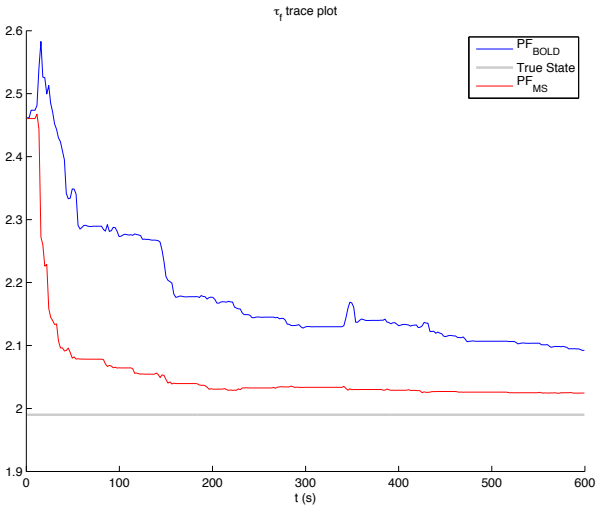

Figure 4.17: τ_f estimate trace plot: Both the filters converge near the true value but the MPF converges earlier ($\sim$200s) and much closer to the true value than the BPF ($\sim 500s$).

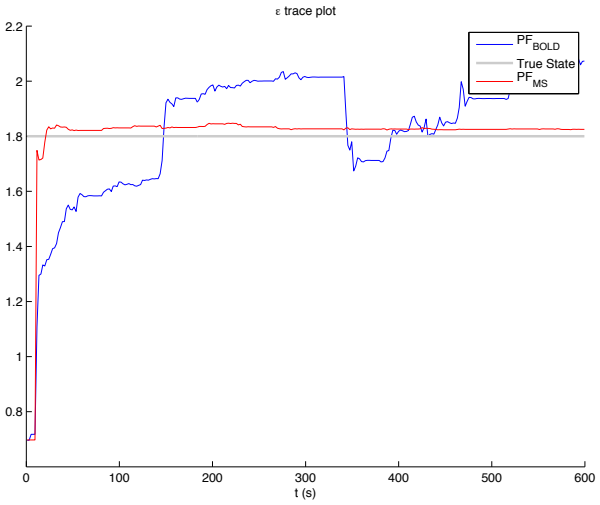

Figure 4.18: ϵ estimate trace plot: Both filters start very far away from the ground truth but the MPF quickly reaches a steady state near the true value. The BPF keeps jumping away from and towards the true value confirming the non-convergence.

4.2.3 Correlation

Even though the parameters start out independent under the prior density, the non-identifiability of the parameters may manifest as a strong correlation among parameters in the posterior density estimates [57]. Correlation between the parameters during a single 600s run was measured using Pearson's product-moment coefficient. The correlation obtained using BPF and MPF is summarized in Tables 4.3-4.5. The BPF parameter estimates show significant correlation because of the overparameterized BOLD model. Using the MPF, the correlation between the parameter estimates is reduced. It can be argued that low correlation (and hence reduced for the MPF case) can be a result of the dominance of true posterior by the prior [57] but it is shown in Section 4.4 that the MPF has, in fact, reduced sensitivity to priors. Thus, this reduction in the correlation can be accounted for by the introduction of the additional observations - CBF and CBF.

Table 4.3: Lower triangular matrix of the parameter correlation coefficients for BPF estimates.

	τ_0	α	E_0	V_0	τ_s	τ_f	ϵ
τ_0	1						
α	-0.9776	1					
E_0	-0.9799	0.9848	1				
V_0	0.818	-0.8754	-0.8476	1			
τ_s	0.7465	-0.7206	-0.6731	0.6004	1		
τ_f	-0.856	0.7898	0.8586	-0.5018	-0.4816	1	
ϵ	-0.6793	0.7556	0.6963	-0.9626	-0.5947	0.2739	1

Table 4.4: Lower triangular matrix of the parameter correlation coefficients for MPF estimates.

	τ_0	α	E_0	V_0	τ_s	τ_f	ϵ
τ_0	1						
α	-0.4815	1					
E_0	0.0127	-0.2953	1				
V_0	-0.2696	-0.1419	0.1339	1			
τ_s	0.03375	0.2113	-0.5948	-0.4055	1		
τ_f	-0.4598	0.7015	0.0186	-0.0074	0.339	1	
ϵ	0.1761	-0.2785	0.1744	0.1448	-0.6262	-0.5184	1

Table 4.5: Net change in correlation coefficients of the parameter estimates from Table 4.3,4.4. Positive values indicate that the correlation of the MPF has decreased compared to the corresponding parameter correlation value for the PF estimate, negative values indicate otherwise.

	τ_0	α	E_0	V_0	τ_s	τ_f	ϵ
τ_0							
α	0.4961						
E_0	0.9672	0.6895					
V_0	0.5484	0.7335	0.7137				
τ_s	0.7128	0.5093	0.07824	0.1949			
τ_f	0.3963	0.08832	0.84	0.4943	0.1426		
ϵ	0.5032	0.4771	0.5219	0.8781	-0.03146	-0.2445	

4.2.4 Accounting for the Additional Information

It can be argued that since the MPF effectively observes 3 times more data than the BPF, giving a 3x longer measurement to the BPF will be a fair comparison. To test this, the BPF was run with a 1800s long measurement, which can be considered to be the same as using a 600s measurement of BOLD , CBV w and CBF w each for the MPF. It can be seen from Figs. 4.19-4.25 that the estimates for a longer (1800s) measurement have their means closer to the ground truth compared to the normal (600s) BPF estimates but still not better than MPF (except τ_0 and E_0). Notably, the variance of the estimates still does not decrease for the 1800s measurement case of the BPF compared to normal case with a 600s run (except ϵ and marginal reduction for V_0).

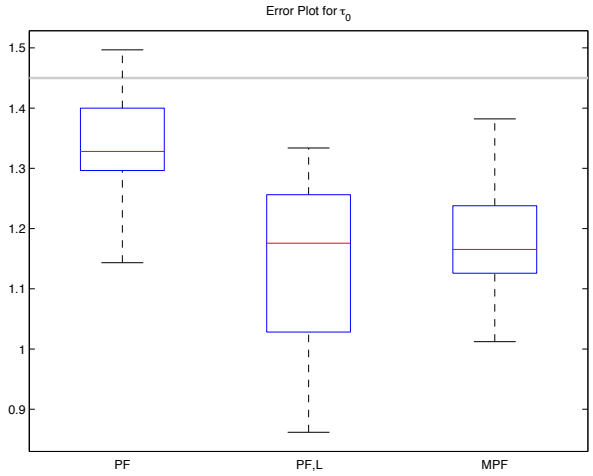

Figure 4.19: τ_0 estimates accounting for additional information: The additional information from the long measurements does not really help the τ_0 estimate. This can be attributed to the non-convergence of the BPF τ_0 estimate.

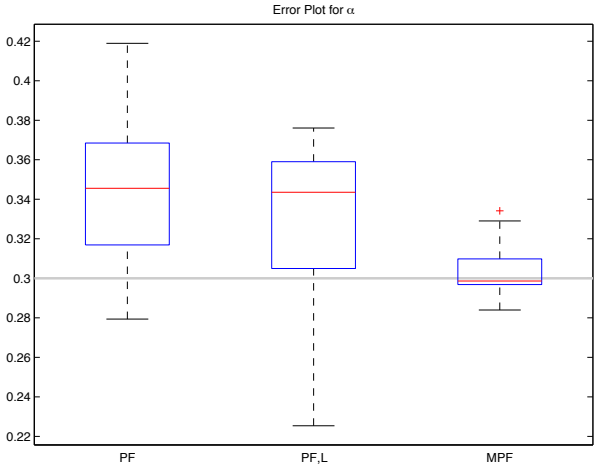

Figure 4.20: α estimates accounting for additional information: The MPF estimates are still better with smaller variance and mean closer to ground truth.

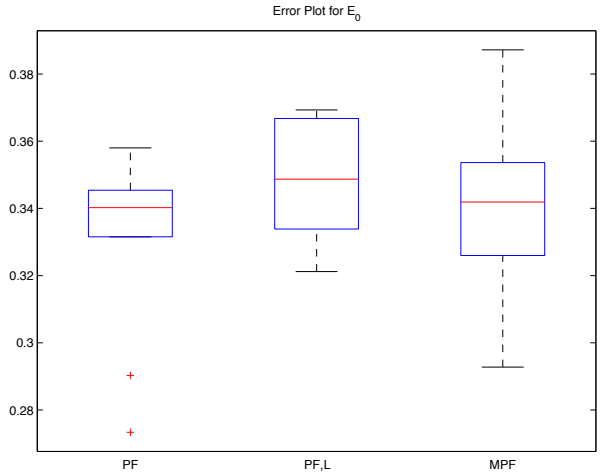

Figure 4.21: E_0 estimates accounting for additional information: The long version estimates do not improve on the regular BPF estimates.

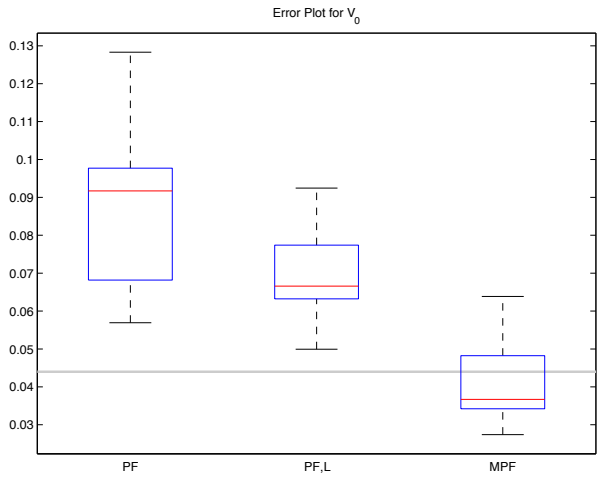

Figure 4.22: V_0 estimates accounting for additional information: The longer version has smaller variance and mean closer to the true value than the regular BPF. Still, the MPF estimates are closer to the true value.

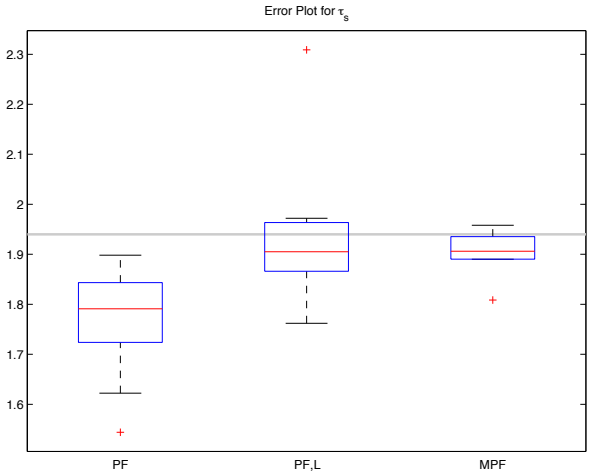

Figure 4.23: τ_s estimates accounting for additional information: The longer version has the mean of the estimates closer to the true value than the regular BPF on account of better convergence. The MPF estimates still have smaller variance.

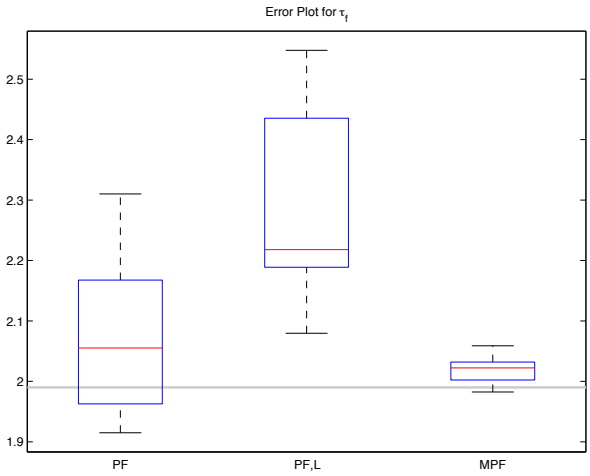

Figure 4.24: τ_f estimates accounting for additional information: In this case, the additional information actually worsens the estimates. This suggests that with non-convergence, the estimates might actually end up further away from ground truth rather than closer to it.

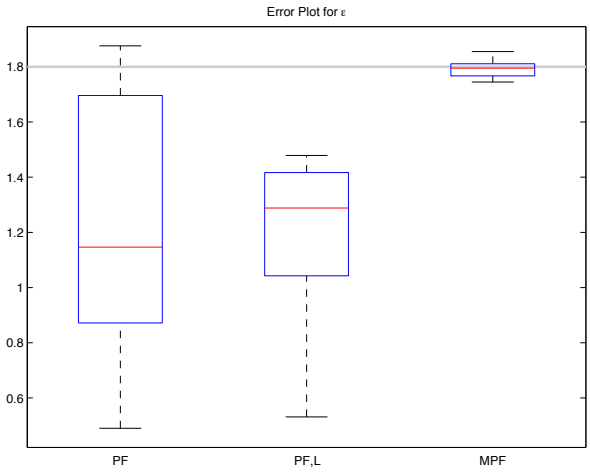

Figure 4.25: ϵ estimates accounting for additional information: The longer BOLD measurement parameter estimates are more biased compared to the regular version by decreasing the variance. But these estimates are still away from the true value and does not outperform MPF.

4.3 Robustness Against Noise

With the use of additional information, we can expect the MPF to be more robust against noise than the BPF. To test this, random additive Gaussian noise (AGN) was added with 3 σ_N (standard deviation of the noise) levels - N1: high SNR = 50dB , N2: medium SNR = 25dB and N3: low SNR = 5dB. This noise was added to the BOLD , CBV and CBF measurements and input to the BPF and MPF with the following combinations (Fig. 4.26-4.28) :

1. Noisy BOLD
2. Noisy CBV (in MPF)
3. Noisy CBF (in MPF)
4. Noisy BOLD , CBV and CBF

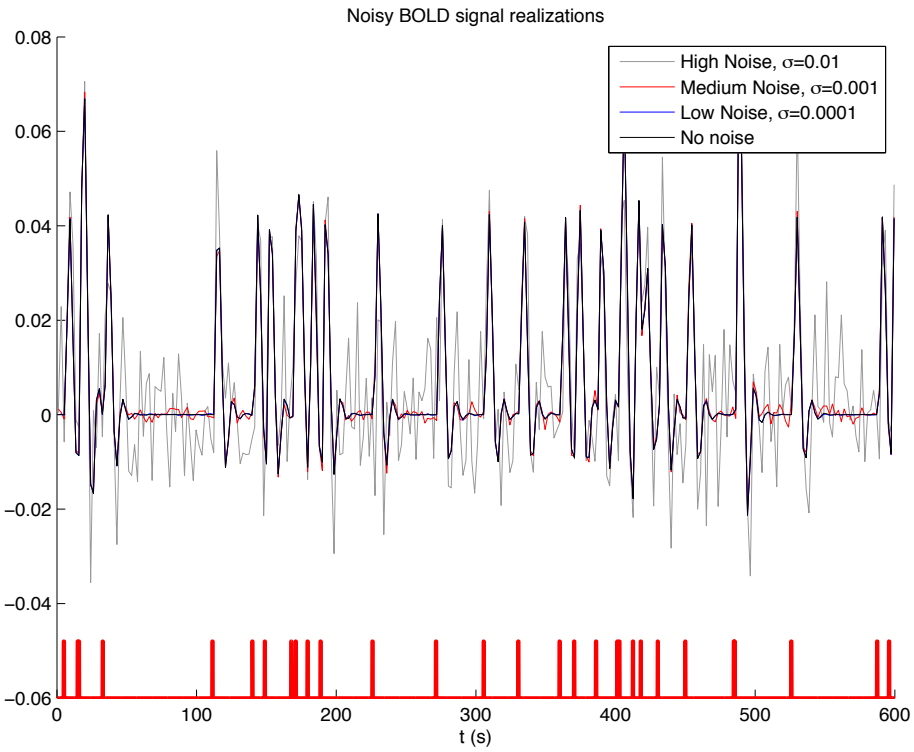

Figure 4.26: Noisy BOLD signal realization for a single voxel for a 600s long, block-stimulus (0.5s duration) input (shown at the bottom of the plot) with the 3 noise levels. For N1 - $\sigma_N = 0.0001$, N2 - $\sigma = 0.001$ and high noise case N3 - $\sigma = 0.01$.

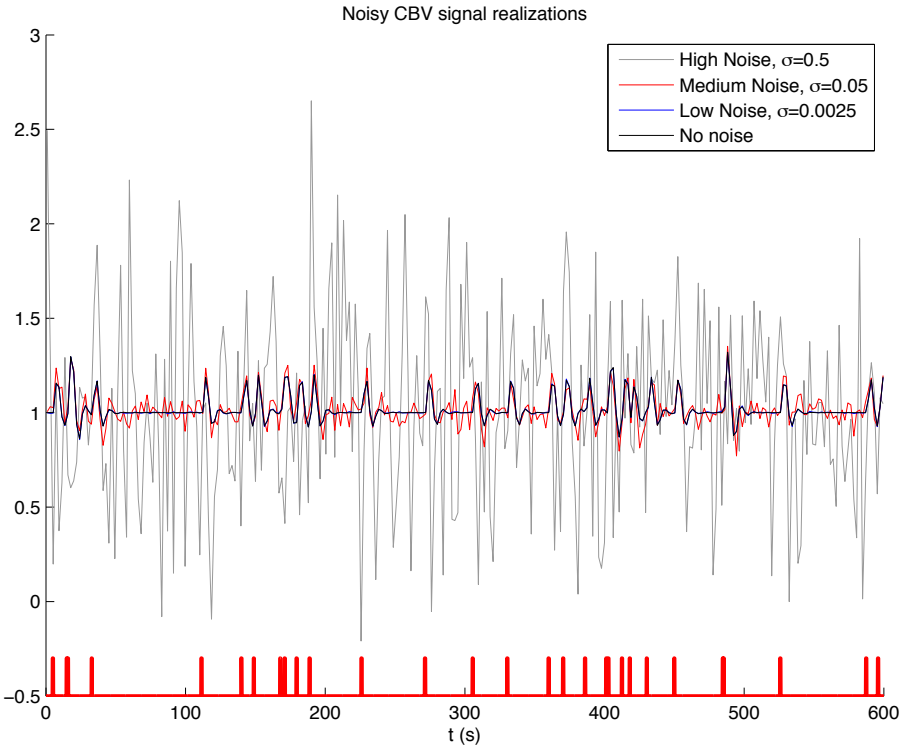

Figure 4.27: Noisy CBV signal realization for a single voxel for a 600s long, block-stimulus (0.5s duration) input (shown at the bottom of the plot) with the 3 noise levels. For N1 - $\sigma_N = 0.0025$, N2 - $\sigma = 0.05$ and high noise case N3 - $\sigma = 0.5$. The σ in these cases are higher because the normalized value of the CBV is more than the BOLD signal. Hence in order to maintain the same SNR, higher levels of σ were added.

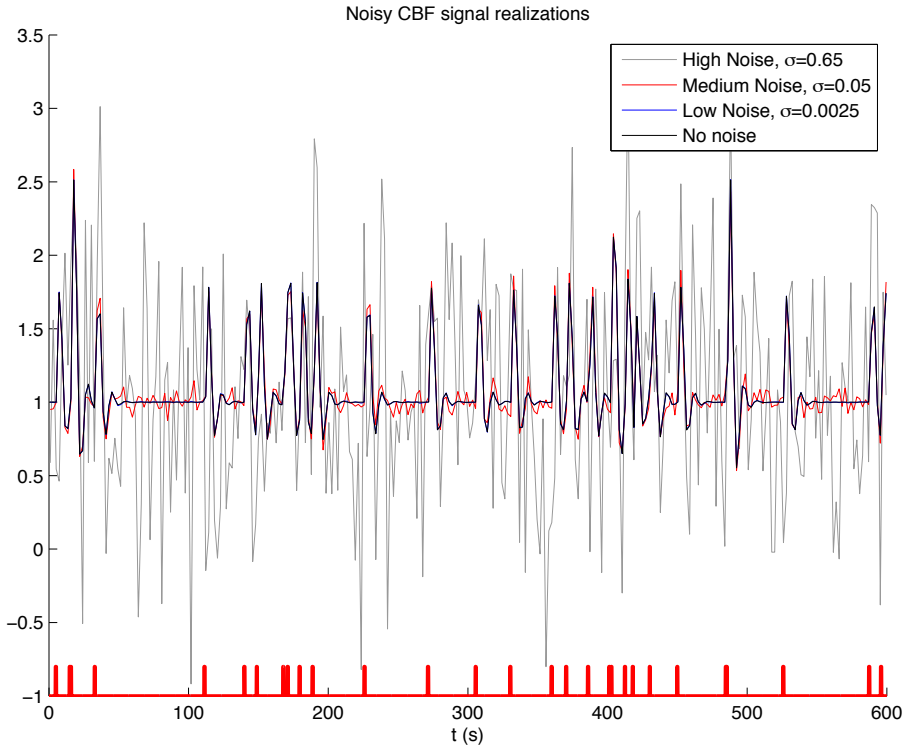

Figure 4.28: Noisy CBF signal realization for a single voxel for a 600s long, block-stimulus (0.5s duration) input (shown at the bottom of the plot) with the 3 noise levels. For N1 - $\sigma_N = 0.0025$, N2 - $\sigma = 0.05$ and high noise case N3 - $\sigma = 0.65$. The σ in N3 level is higher to take into account the slightly higher normalized value of CBF and to maintain the same SNR for this level

As can be seen from the boxplots (Figs.4.29-4.35), the MPF estimates have much less error than the BPF estimates for each corresponding combination listed above. Also, the variance of the estimates obtained using MPF does not flare up anywhere as much as the BPF estimates except for the N3 level. In these figures, the 4 plots clockwise from top left are - Noisy BOLD; Noisy CBV; Noisy BOLD , CBV , CBF; Noisy CBF.

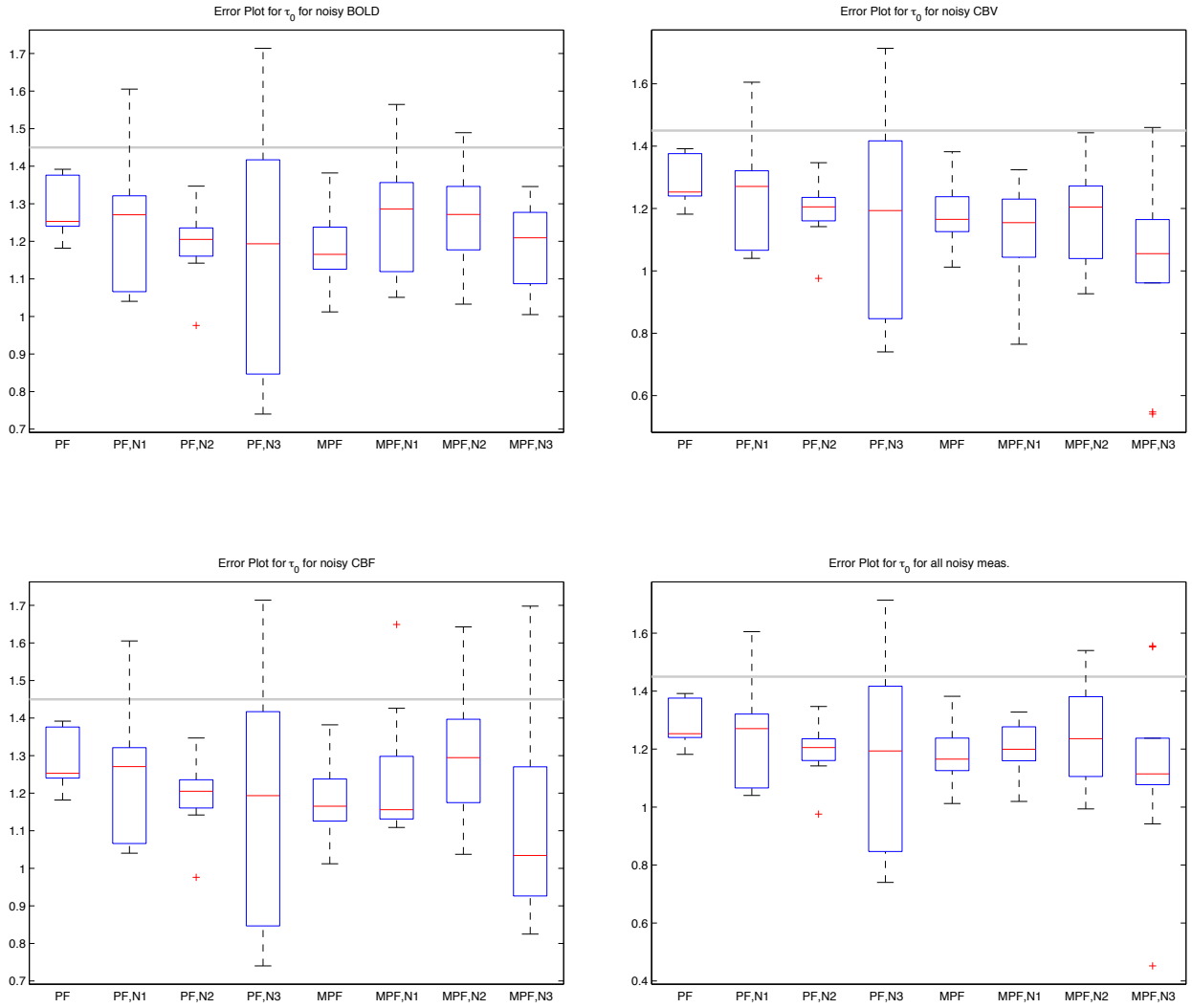

Figure 4.29: τ_0 estimates for the 4 cases with 3 noise levels: The variance for the BPF estimates increases with increasing noise levels and is quite bad for N3. For the MPF, the variance does not increase as much.

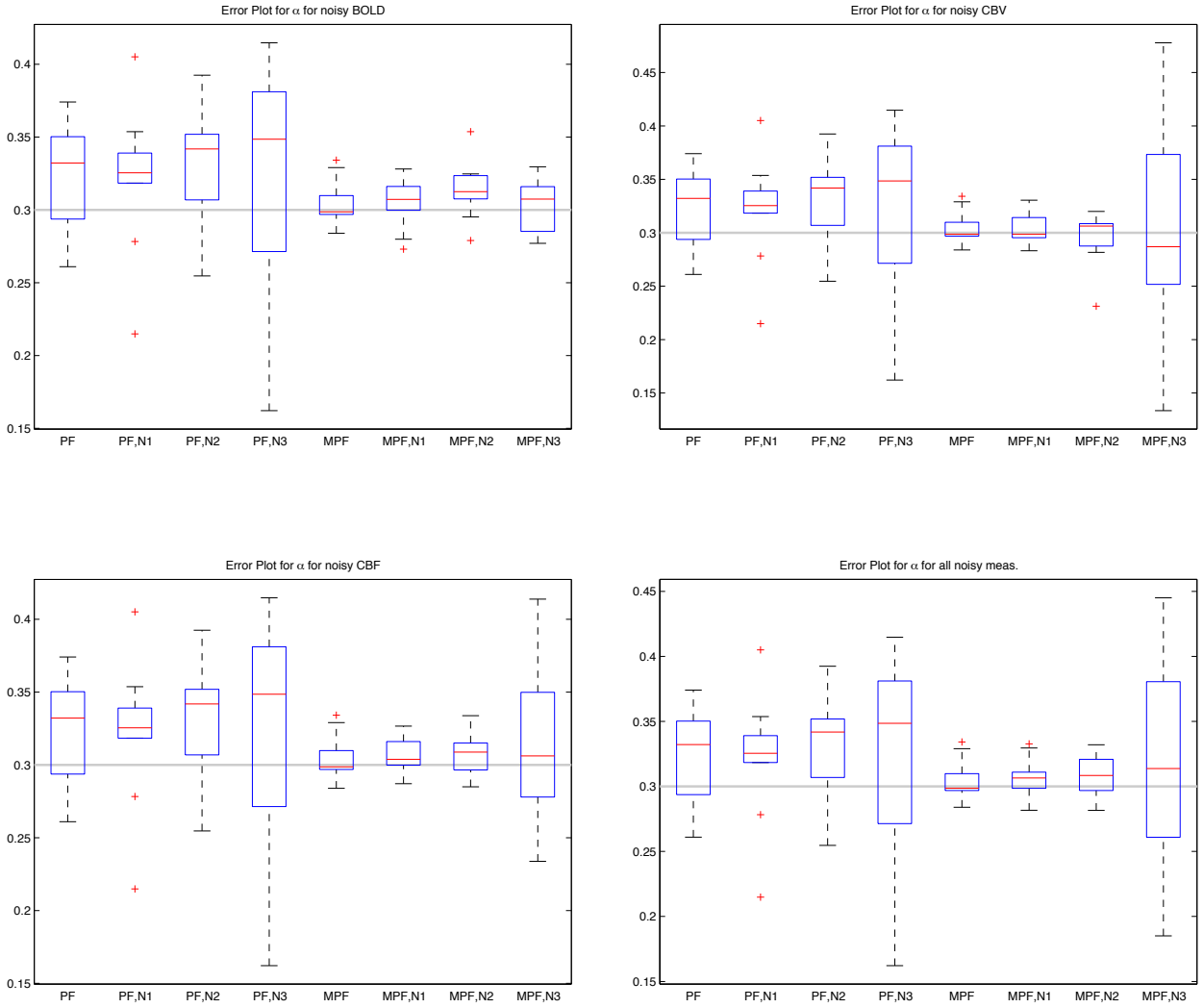

Figure 4.30: α estimates for the 4 cases with 3 noise levels: The variance for the BPF estimates increases with the noise levels as does the mean estimation error. For MPF case, the variance is high only for the N3 level while the mean of estimates values is closer to the true value.

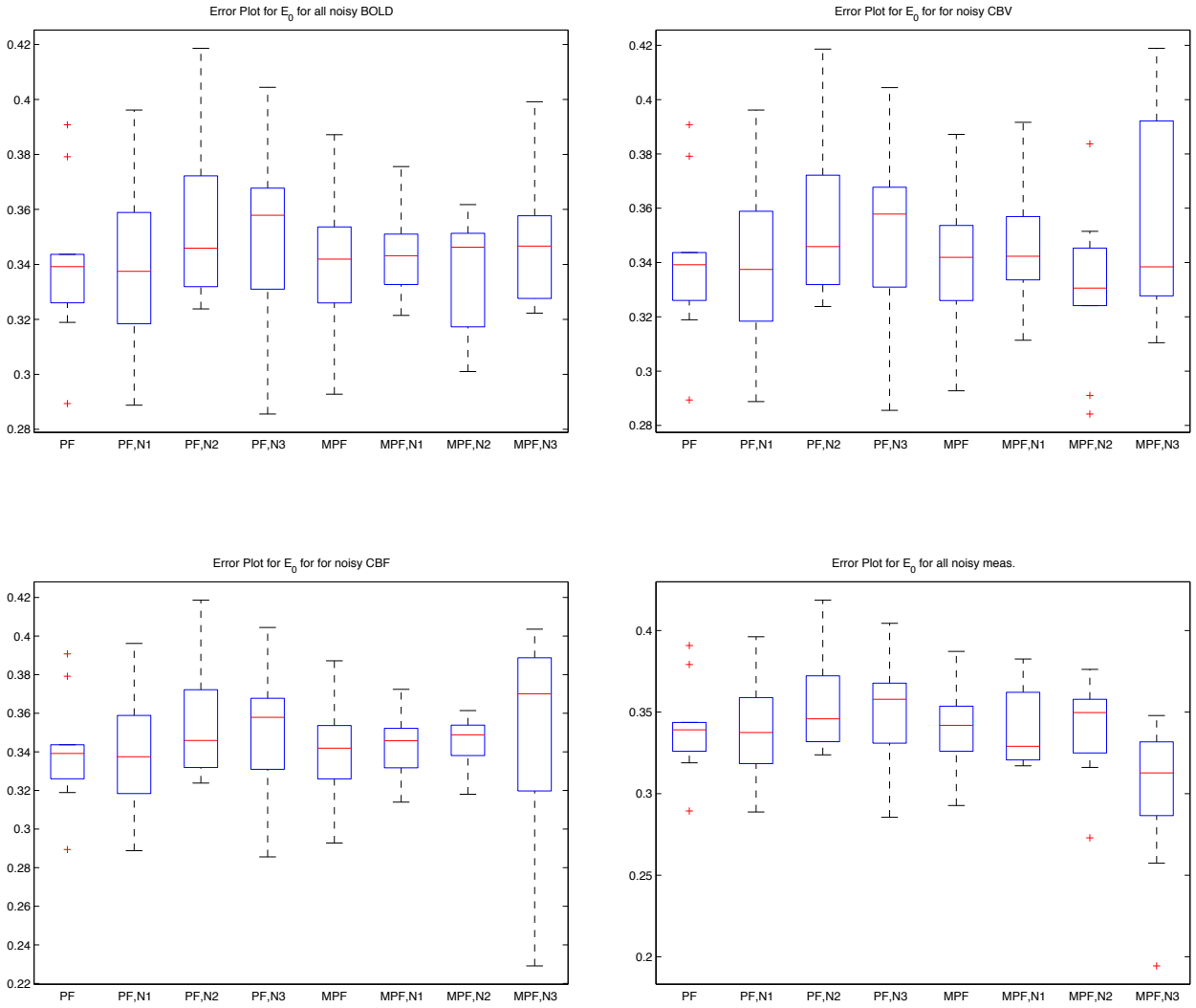

Figure 4.31: E_0 estimates for the 4 cases with 3 noise levels: The parameter estimates have increased variance and median estimate error with increasing noise levels. The deterioration is about the same for all the cases. It can be seen that the estimates seem to improve for noisy CBF measurements but it is mainly due to added uncertainty by the noise.

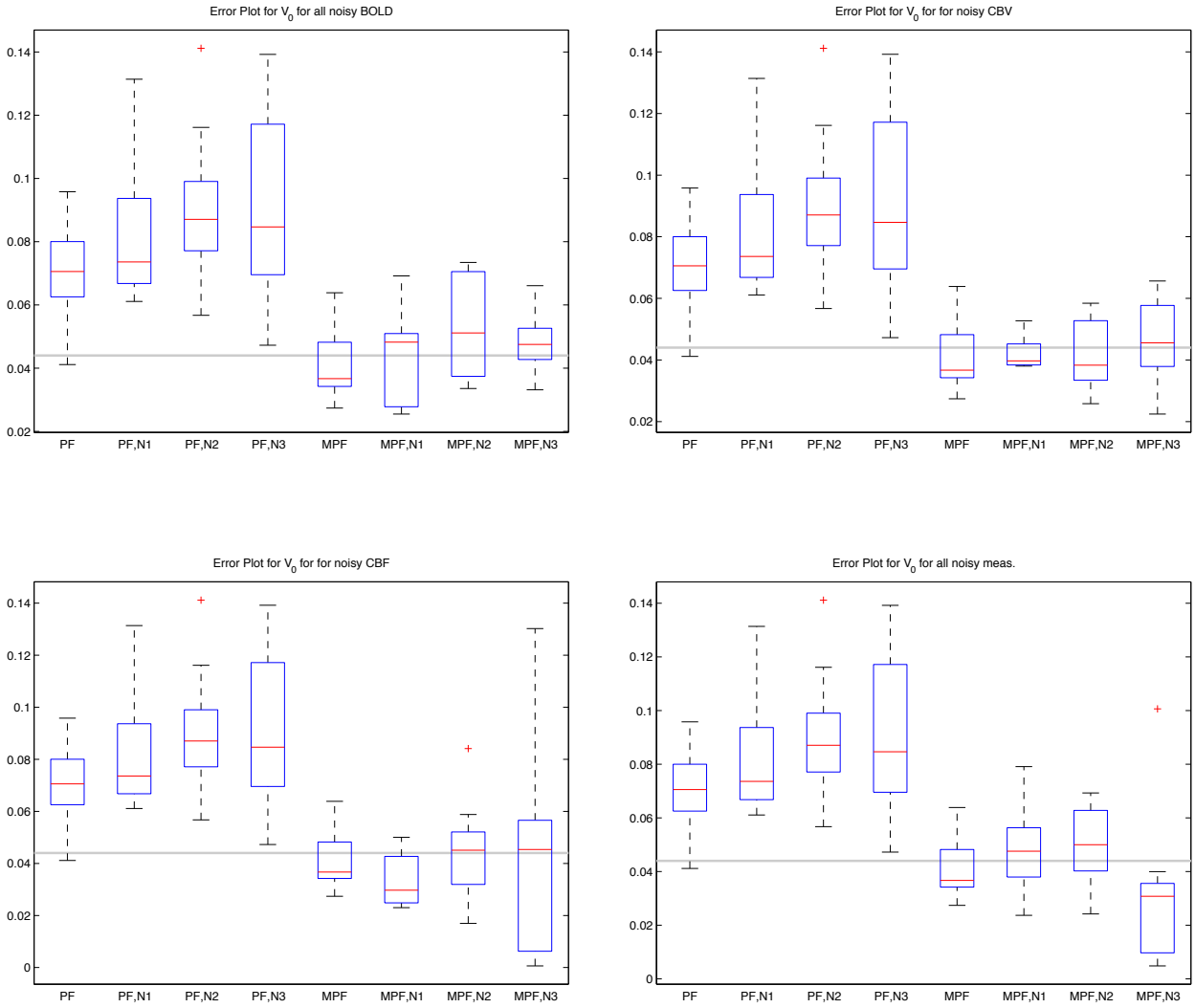

Figure 4.32: V_0 estimates for the 4 cases with 3 noise levels. This parameter is the most sensitive to the BOLD measurement as it enters the equation through the measurement itself. With increasing noise, the variance for the BPF estimates blows up. For the corresponding noise levels with the MPF estimates, the variance does not increase but the median values are off slightly as the CBV and CBF measurements help correct the weighting function.

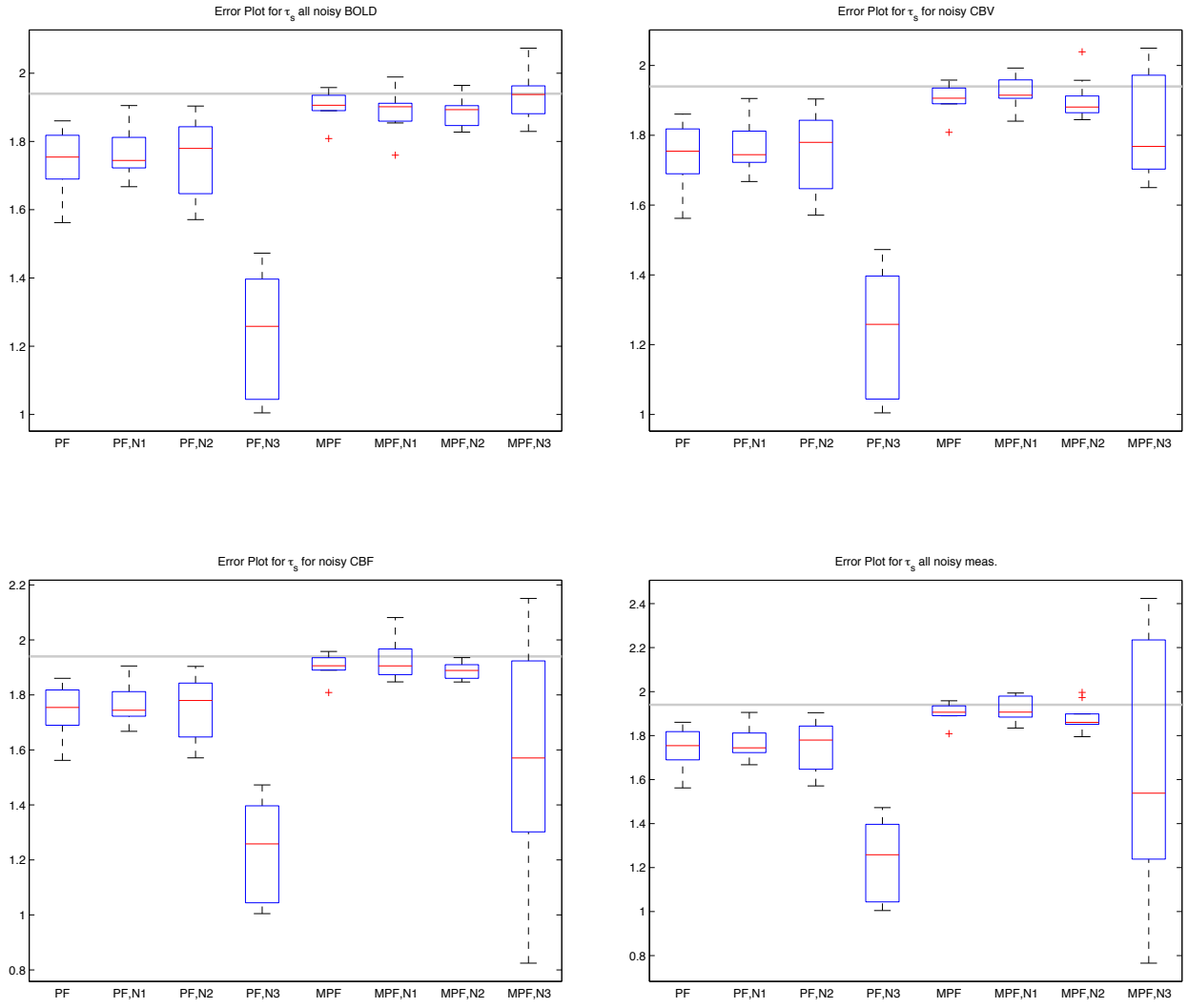

Figure 4.33: τ_s estimates for the 4 cases with 3 noise levels. The BPF estimates keep worsening with increasing levels of noise. Particularly for the N3 level, there is a large increase in variance and the mean is completely off the true value. With MPF, the estimates hold up pretty good except for the high noise case of the CBF and all noisy measurement since this parameter enters the system through CBF measurement.

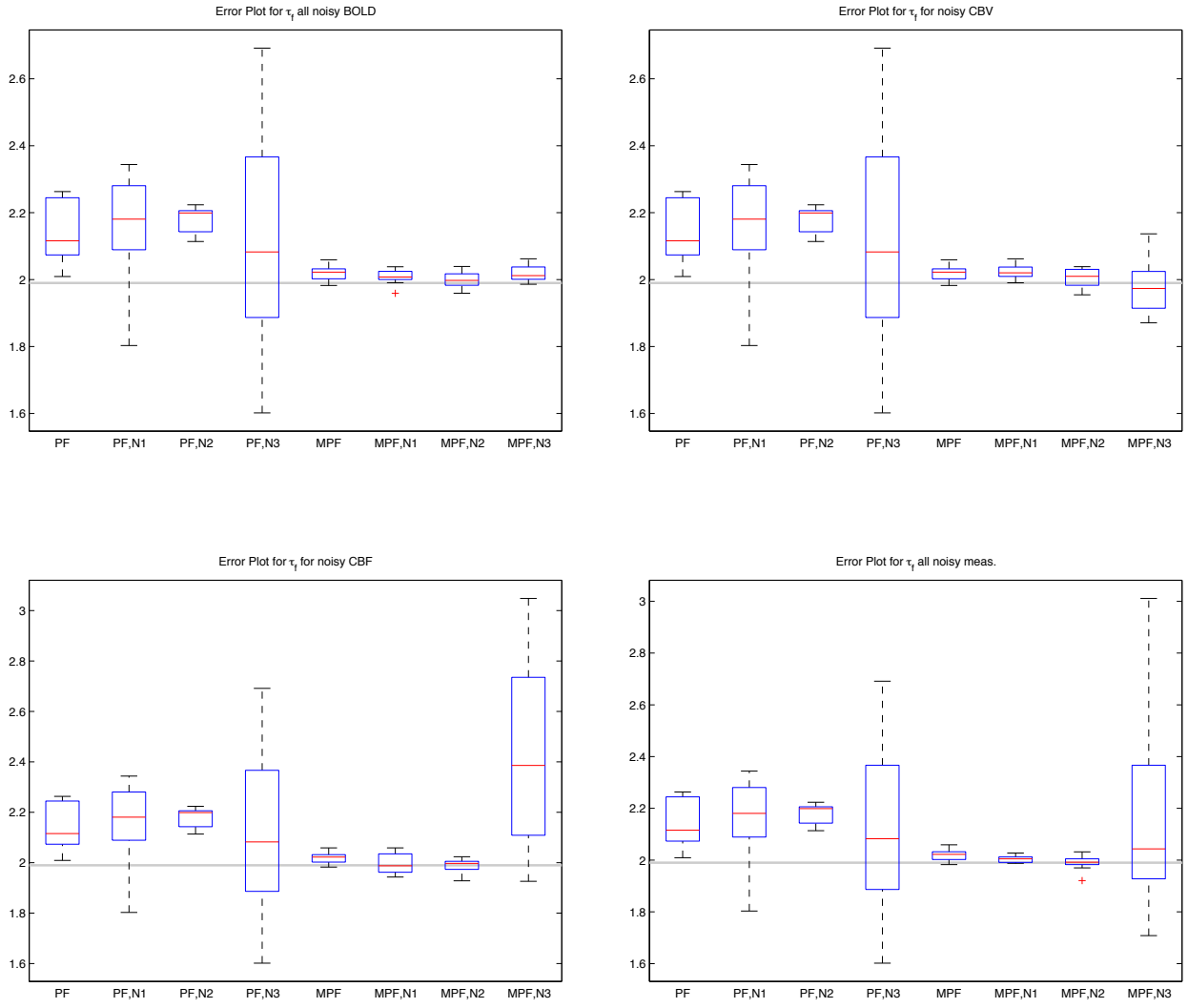

Figure 4.34: τ_f estimates for the 4 cases with 3 noise levels. Similar to the previous parameter τ_s, τ_f enters the system through CBF measurement and the trend is similar with increasing noise.

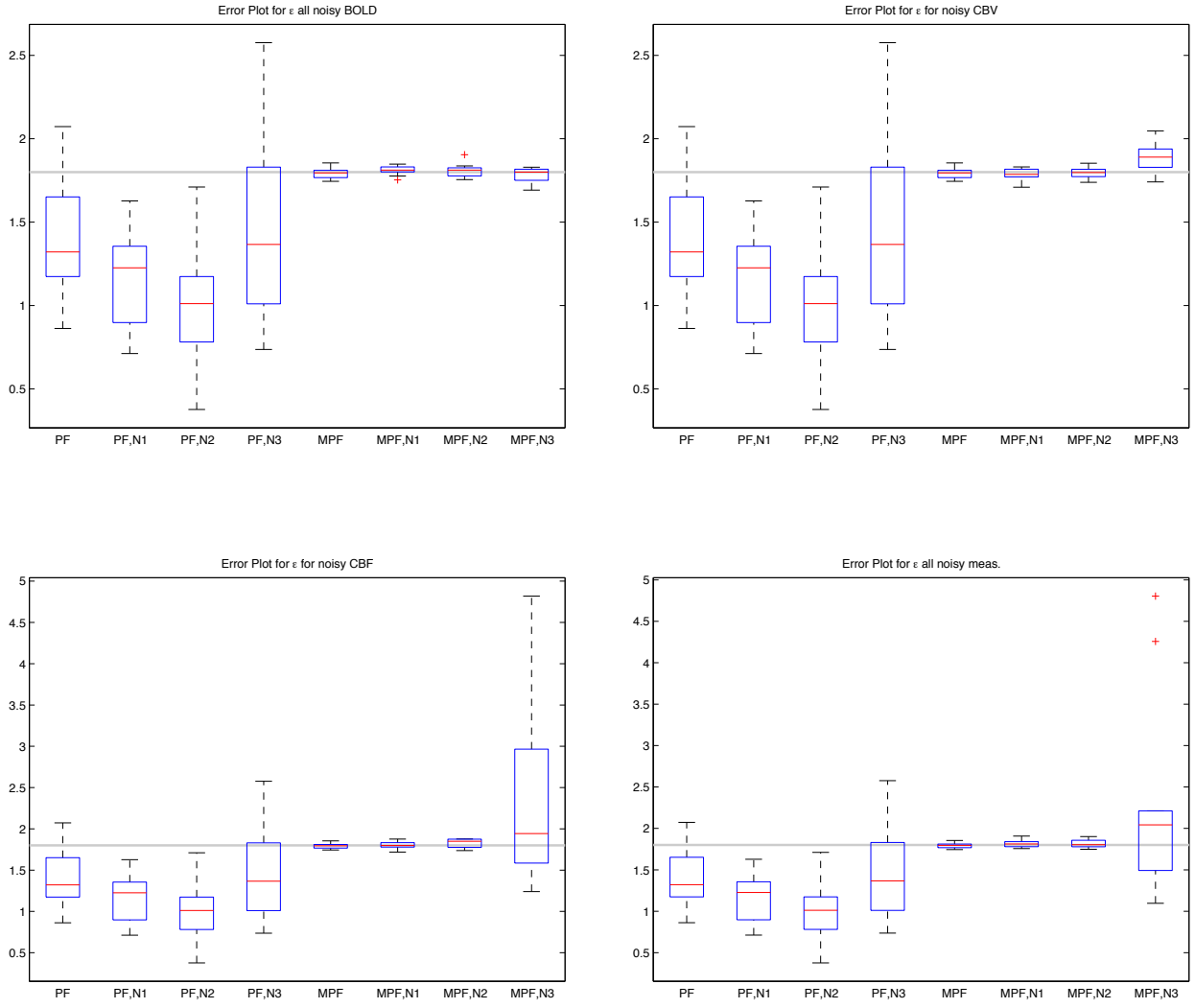

Figure 4.35: ϵ estimates for the 4 cases with 3 noise levels. Similar to the previous 2 parameters, ϵ enters the system through CBF meas. The variance blows up rapidly with increasing noise levels for the BPF estimates whereas the MPF estimates again maintain the variance and mean values except for the high CBF noise case.

4.4 Sensitivity to Priors

In a PF, choice of the prior distribution of the parameters to be estimated influences the final estimates of the parameters [2]. In the case of an overparameterized model, the PF will be more

Table 4.6: Parameter Values to test sensitivity to prior: P-Δ_{25} and P+Δ_{25} correspond to 25% deviation from the original.

Parameter set	τ_0	α	E_0	V_0	τ_s	τ_f	ϵ
Original	1.45	0.3	0.47	0.044	1.94	1.99	1.8
P-Δ_{25}	1.0875	0.22	0.3525	0.033	1.45	1.49	1.35
P+Δ_{25}	1.81	0.375	0.5875	0.055	2.425	2.487	2.25

Table 4.7: Estimation error for different parameter values with the same prior.

Parameter set	Filter	τ_0	α	E_0	V_0	τ_s	τ_f	ϵ
Original	PF	19.48	12.12	27.61	61.57	10.28	7.437	24.78
Original	MPF	18.62	3.527	27.66	24.85	2.075	1.595	1.348
P-Δ_{25}	PF	41.52	46.08	5.334	67.97	5.484	32.95	38.34
P-Δ_{25}	MPF	13.79	25.96	7.065	40.38	10.73	11.78	12.26
P+Δ_{25}	PF	23.64	14.62	41.68	120.1	37.96	13.46	42.06
P+Δ_{25}	MPF	30.29	5.225	42.61	22.89	8.634	1.628	4.234

sensitive to the priors [57]. To test this 3 different sets of parameters were used as ground truth to simulate a voxel of the BOLD , CBV w and CBFw measurements each:

Table 4.7 summarizes the error in the estimates using the BPF and MPF with the four parameter sets listed in Table 4.6. It can be seen that using the same values of priors for a different set of parameters values does influence the final estimates. This influence is seen more in the estimates obtained using the BPF than the MPF estimates. The sensitivity of the parameters to the priors is reduced in the case of MPF as the variation in the final estimates is not as drastic as the BPF final estimates.

4.5 Number of Particles

In a PF, the more the number of particles used, the better is the approximation of the posterior density but at the cost of additional computational time. The effect of decreasing the number of particles is seen in the increased variance of the posterior distribution of the estimates due to the non-convergence. This effect was tested with the BPF and the MPF estimates. The results (Figs. 4.36-4.42) show that as the number of particles (N_s) decreases, the BPF estimates' variance increases more than that of the MPF estimates. For the BPF, the estimates' mean deviates more from the ground truth whereas for the MPF, the mean is considerably off only for $N_s = 50$. This shows that with decreasing N_s, the MPF estimates do not worsen as much as the BPF estimates

Table 4.8: Parameter estimation error with decreasing N_s

Filter	N_s	τ_0	α	E_0	V_0	τ_s	τ_f	ϵ
PF	50	23.24	49.32	32.64	82.48	14.18	10.98	25.71
MPF	50	93.36	13.61	21.58	164.6	7.937	3.554	5.537
PF	100	25.69	17.58	27.92	101.7	10.95	16.86	40.9
MPF	100	15.59	7.413	27.24	31.46	5.046	2.808	3.087
PF	500	20.72	13.03	27.04	81.05	11.82	12.22	34.47
MPF	500	18.57	5.824	27.84	37.34	2.417	2.002	1.71
PF	1000	15.29	14.11	28.24	76.8	10.72	9.697	28.52
MPF	1000	17.72	5.328	26.26	28.68	3.261	1.851	2.264

because even with a smaller number of particles, the additional information from the CBV and CBF measurements provides a better posterior distribution coverage by updating the weighting function better and assigning importance to the particles.

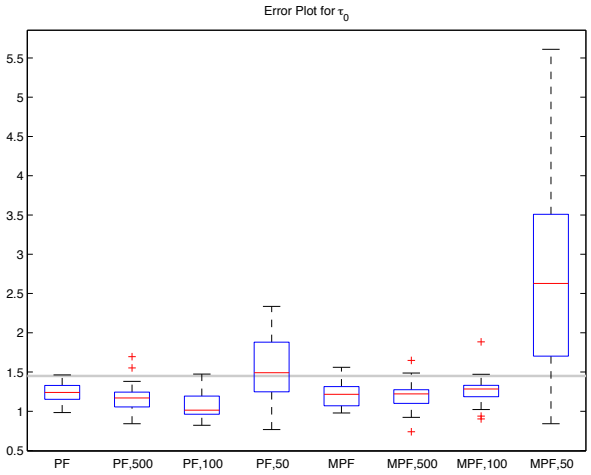

Figure 4.36: τ_0 estimates with decreasing number of particles: With fewer particles, the MPF estimates hold up quite well except for N_S=50. For the BPF, the estimates worsen gradually although the performance for N_s=50 is not as bad.

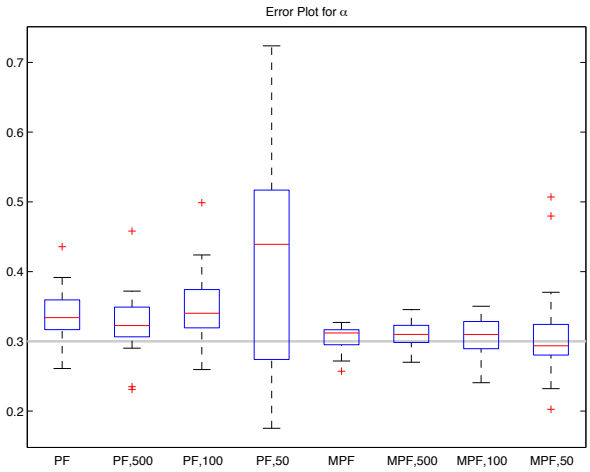

Figure 4.37: α estimates with decreasing number of particles: The MPF estimates' variance increases gradually but the mean stays the same. For the BPF, the mean keeps worsening and the estimates for N_s=50 are poor - large variance and mean shifted from the true value.

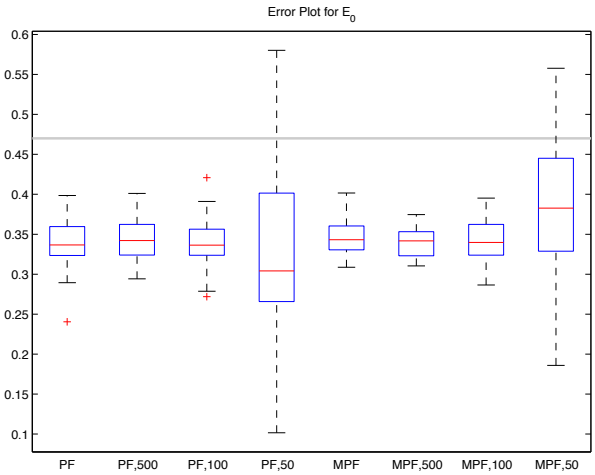

Figure 4.38: E_0 estimates with decreasing number of particles: For the both BPF and acMPF the effect is quite similar - mean and variance are the same except for the N_s=50 case where the variance increases drastically.

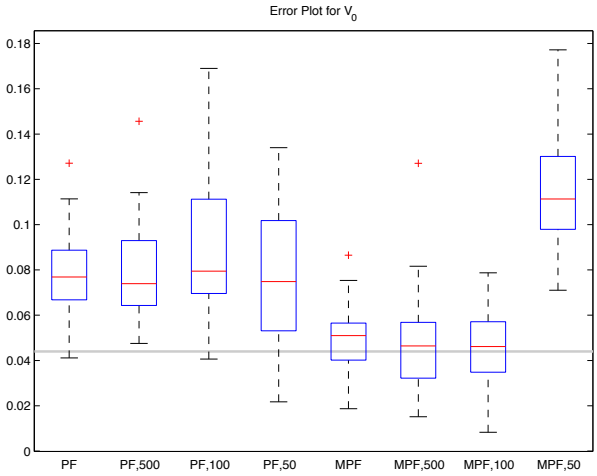

Figure 4.39: V_0 estimates with decreasing number of particles: The BPF estimates worsen with fewer particles. The MPF estimates are consistent until N_s=50.

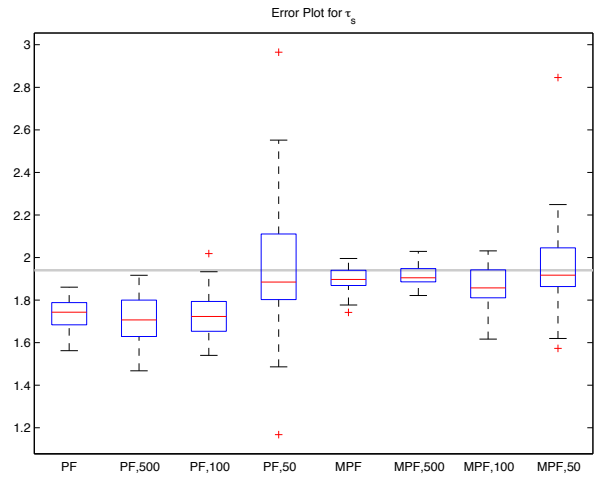

Figure 4.40: τ_s estimates with decreasing number of particles: The estimates for both BPF and MPF are quite consistent for N_s=1000 and 500. For N_s=50, the BPF estimates exhibit higher variance.

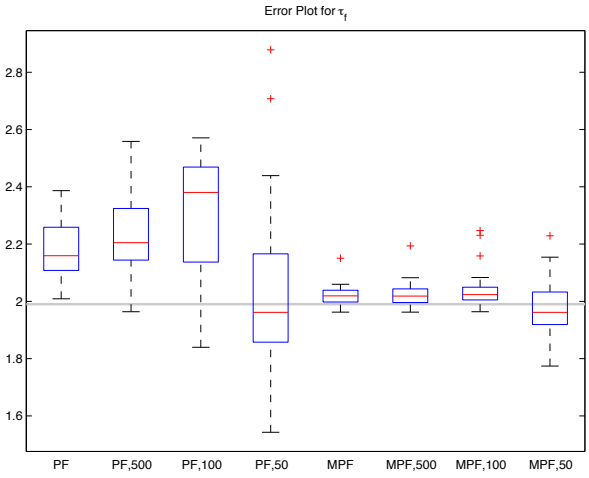

Figure 4.41: τ_f estimates with decreasing number of particles: The BPF estimates deteriorate quickly with decreasing N_s. Even though the mean is close to ground truth for N_s=50, the variance is quite high. The MPF estimates are also consistent for N_s=1000 and 500 but the variance increases for N_s=50.

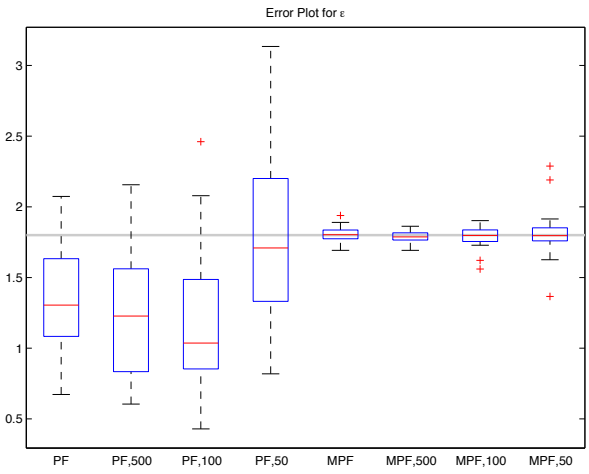

Figure 4.42: ϵ estimates with decreasing number of particles: The BPF estimates have their mean shifted more from ground truth with decreasing particles. The variance for N_s=50 is really high. Comparatively, the MPF estimates are much more consistent form N_s=1000 to 50.

Chapter 5

Discussion

5.1 Overview of the Parameter Estimates

5.1.1 E_0

Of all the parameters, neither the CBV nor the CBF add any more information about E_0 than the BOLD signal. As expected there was no considerable improvement in the estimates of this parameter in the tests. Even for the prior sensitivity test, the influence of the prior on the E_0 estimate was the same for both BPF and MPF. The variance of this estimate with MPF does not increase as much as it does for the BPF when the $N_s = 50$. Again, this reduction is not significant enough to arrive at any conclusion.

5.1.2 τ_0 and α

α estimates have significantly reduced in the mean error ($\sim 4\%$) and variance. This can be accounted for by the fact that additional information about it enters the BOLD model (1.2) through the volume (v) and the deoxyhemoglobin content (q) of which we are measuring only v through CBV.

τ_0 is one parameter which did not show any improvement in the quality of the estimate - mean or variance - through all the tests except for marginally reduced and steady variance during noise tests and steady mean estimates with fewer particles. Additionally the steady trace plot for the MPF estimate indicated that the parameter had indeed converged although to a value quite different from ground truth.

5.1.3 V_0

This parameter is the most sensitive to the nature of BOLD signal since it enters the model only through the output equation. With the decreased dependence of the MPF on the BOLD signal measurement to update the weights, this sensitivity is markedly decreased for the MPF parameter estimates considering that the actual value of this parameter (0.044) is almost a magnitude lower than the next lowest value ($\alpha = 0.3$). In all the tests (except $N_s = 50$), the error in the mean of the MPF estimates did not vary compared to the BPF.

5.1.4 ϵ, τ_s and τ_f

These 3 parameters are part of the rCBF component of the BOLD model which are estimated through the CBF alone and show marked improvement in their estimates using the MPF. Notably, the variance in the MPF estimates of these parameters was reduced quite sharply in comparison to the BPF estimates. The variance also did not deteriorate as much with increasing levels of noise and fewer particles.

5.2 Identifiability of Parameters

The model for the BOLD effect, first introduced by [53] and extended by [13] has come a long way in modeling the various aspects of the BOLD signal observed. Of these models, the Balloon-Windkessel Model proposed independently by [7] and [48] respectively and further refined by [22] to give model linking the input stimulus to the BOLD response seen forms the basis of most of the models used today. Though there have been several enhancements to this Balloon Model [6] which introduce various new parameters to better capture the dynamics of the BOLD signal, the sensitivity analysis done by Deneux and Faugeras [14] suggests that the newer BOLD models proposed are overparameterized and the model by Friston et al. [22] is sufficient to capture most of the necessary aspects. The parameter correlations seen by Chambers et al. [9] indicate that estimating parameters from this BOLD model is an ill-posed inverse problem. The trace plots of the parameter estimates exhibit slow convergence and trending which can be attributed to the correlations among parameters for an overparameterized model [57]. Using additional information about the model - volume (v) from the CBVw VASO [44] or VASO-FLAIR [17] and the blood flow (f) from the CBFw ASL [61] - the correlation between the parameters decreases and the trace plots of the estimates show better convergence.

5.3 Influence of Priors

In a Bayesian inference scheme like the PF, priors for the parameters influence the final estimates. It is viewed as a drawback but it is much more intuitive to make assumptions about the data by taking into account its nature or underlying distribution. In this work, the gamma priors for the parameters make sure that there are no negative values since they are meaningless for the physiological parameters. When a model reduction method is employed, the parameters will lose their physical meaning and the task of assigning priors to the new reduced set of parameters will be much more complicated. However, the importance of priors has to be considered [2] which is certainly more for an overparameterized model like the BOLD model. Using the same priors for different sets of ground truth values of the parameters might be a problem for a BPF scheme which requires some trial-and-error procedure to ensure optimal performance. This problem is handled much better in the MPF since it relies not only on the BOLD signal measurement to arrive at a better posterior distribution of the parameters but also uses the CBV and CBF measurements to update the particle weights and increase the robustness of the posterior density. However, even the MPF procedure is to a certain extent sensitive to the choice of prior and remains an important part of the design of the PF.

The influence of choice of the prior on parameter error also suggests that there might be one unique set of priors which gives an optimal solution to the parameter identification problem. Although this can be a cause for concern, with MPF this problem is mitigated and the dependence on finding the unique set is not crucial.

5.4 Effect of Noise

Noise in measurements leads to a reduction in the sensitivity of the contrasts. This, in turn, will lead to poorer estimates of the parameters. Usually the BOLD, CBF and CBV images are acquired between N1 and N2 noise levels. With these noise levels, the performance of both BPF and MPF is quite acceptable. The mean of a parameter estimate is the value which will generally be used to arrive at some conclusion about that parameter. BPF estimates starts going off from the true value with increasing noise. The MPF estimates hold their ground better in this respect. The MPF estimates have better variance i.e. the lower variances indicate that the chance of a random error in estimation will be lower. This directly bears a relation to better convergence and overall estimation performance of the MPF.

5.5 Number of Particles

A particle in a PF contains all the information about the variable required to run it. The larger the number of particles, the closer the approximation will be to the actual density. However, the

computational complexity will increase drastically with the number of particles and more so with the dimensions of the model [11]. The choice of the number of particle (N_s) to be used is more of a trial and error process than a rule of thumb. It is seen that the MPF performance with even 100 particles is almost as good as that with 1000 particles - the mean estimation error not changing more than 5% and the variance also remaining the same. For the BPF, the mean estimation error increases accompanied by increased variance (uncertainty). Thus, with additional information about a model, the dimensionality curse of the PF can be mitigated by keeping the computational complexity in check with fewer particles and no significant effect of the estimates.

5.6 Future Work

5.6.1 Complex Models

The BOLD model (1.2) proposed by Friston et al. [22] accounts for most of the nonlinearities observed in the BOLD response [14]. More complicated models have been proposed to account for a few experimental observations that have not captured by the BOLD model described in (1.2). These models make the use of additional parameters like CMRO2, neural inhibition, inhibitory time constant, inhibitory gain factor etc. which will worsen the parameter identifiability. It is also to be noted that all these newer and complex models may not be correct. The method presented here can be used to validate and analyze the identifiability of these models. Combining field potential measurements like MEG [5] with CBV and CBF data can also be helpful in these analysis tasks [6].

5.6.2 Single Measurement

The main drawback of this method is the sequential measurements of BOLD, CBV and CBF. A 10 min (600s) measurement of each adds up to 30 mins which can be troublesome from a data collection point of view. Woolrich et al. [74] has proposed an approach which uses a nonlinear ASL signal model to infer changes in CBF, R_2^* (transverse relaxation) and M (static magnetization) in a Bayesian framework, where R_2^* relates to the blood oxygenation and volume changes via the BOLD contrast and percentage M changes can be in turn used to infer CBV changes with some assumptions. Although this technique has the potential to infer BOLD, CBV and CBF from a single modality and thus save time, there might be certain disadvantages associated with estimating hemodynamic parameters from this data as now there is inherent uncertainty in the BOLD, CBV and CBF estimates.

From Section 4.2.2, it was seen that the MPF estimates converge well before the end of the measurement process. Taking advantage of this, the measurement process can be shortened for each of the BOLD, the CBF, and the CBV measurements thus reducing the total measurement duration.

5.6.3 Variational Bayes

Among the various Bayesian methods, Variational Bayes (VB) is another method that is gaining popularity to solve nonlinear inverse problems [33, 12, 20, 10]. It will be interesting to see how this method performs compared to a PF since its performance is at par with a MCMC method but with less computational expense. Earlier (Sections 2.2.2) we mentioned that the RBPF scheme does not give any advantage over using a PF and might even add to the computational expense. Smidl and Quinn [65] have come up with a method that makes use of VB to accelerate the filtering process for a PF in a Rao-Blackwellised system. This is another potential solution that can be explored.

5.7 Conclusion

In this work, we have used a Multimodal Particle Filter to estimate the parameters of a nonlinear dynamic model - BOLD model and demonstrated the advantage in multimodal neuroimaging. This BOLD model is overparameterized and parameter identification is an ill-posed inverse problem. These parameter estimates exhibit correlation and are slow to converge. Instead of using just one measurement of the BOLD signal, additional information about the model - volume (v) from the CBVw (VASO or VASO-FLAIR) and the blood flow (f) from the CBFw (ASL) - improves the parameter identifiability of the BOLD model.

Bibliography

[1] Owen J Arthurs and Simon Boniface. How well do we understand the neural origins of the fMRI BOLD signal? *Trends in Neurosciences*, 25(1):27–31, January 2002.

[2] M. S. Arulampalam, S. Maskell, N. Gordon, and T. Clapp. A tutorial on particle filters for online nonlinear/non-Gaussian Bayesian tracking. *IEEE Transactions on Signal Processing*, 50(2):174–188, 2002.

[3] Pradeep K. Atrey, M. Anwar Hossain, Abdulmotaleb El Saddik, and Mohan S. Kankanhalli. Multimodal fusion for multimedia analysis: a survey. *Multimedia Systems*, 16(6):345–379, April 2010.

[4] Fabio Babiloni, Donetella Mattia, Claudio Babiloni, Laura Astolfi, Serenella Salinari, Alessandra Basilisco, Paolo Maria Rossini, Maria Grazia Marciani, and Febo Cincotti. Multimodal integration of EEG, MEG and fMRI data for the solution of the neuroimage puzzle. *Magnetic resonance imaging*, 22(10):1471–6, December 2004.

[5] F. Bieß mann, Sergey Plis, FC Meinecke, Tom Eichele, and K. Muller. Analysis of Multimodal Neuroimaging Data. *IEEE Reviews in Biomedical Engineering*, 4(5):6, 2011.

[6] Richard B. Buxton, Kâmil Uluda, David J. Dubowitz, and Thomas T. Liu. Modeling the hemodynamic response to brain activation. *NeuroImage*, 23 Suppl 1:S220–33, January 2004.

[7] Richard B. Buxton, Eric C. Wong, and Lawrence R. Frank. Dynamics of blood flow and oxygenation changes during brain activation: The balloon model. *Magnetic Resonance in Medicine*, 39(6):855–864, June 1998.

[8] Francois Caron, Manuel Davy, Emmanuel Duflos, and Philippe Vanheeghe. Particle Filtering for Multisensor Data Fusion With Switching Observation Models: Application to Land Vehicle Positioning. *IEEE Transactions on Signal Processing*, 55(6):2703–2719, June 2007.

[9] Micah C. Chambers, Chris L. Wyatt, William T. Baumann, and A. A. Beex. Full Brain Blood-Oxygen-Level-Dependent Signal Parameter Estimation Using Particle Filters. Master's thesis, Virginia Polytechnic Institute and State University, 2010.

[10] M. A. Chappell, A. R. Groves, B. Whitcher, and M. W. Woolrich. Variational Bayesian Inference for a Nonlinear Forward Model. *IEEE Transactions on Signal Processing*, 57(1):223–236, January 2009.

[11] F. Daum and J. Huang. Curse of dimensionality and particle filters. In *2003 IEEE Aerospace Conference Proceedings (Cat. No.03TH8652)*, volume 4, pages 4_1979–4_1993. IEEE, 2003.

[12] J. Daunizeau, K. J. Friston, and S. J. Kiebel. Variational Bayesian identification and prediction of stochastic nonlinear dynamic causal models. *Physica D. Nonlinear phenomena*, 238(21):2089–2118, November 2009.

[13] T. L. Davis. Calibrated functional MRI: Mapping the dynamics of oxidative metabolism. *Proceedings of the National Academy of Sciences*, 95(4):1834–1839, February 1998.

[14] Thomas Deneux and Olivier Faugeras. Using nonlinear models in fMRI data analysis: model selection and activation detection. *NeuroImage*, 32(4):1669–89, October 2006.

[15] Colin P. Derdeyn. Variability of cerebral blood volume and oxygen extraction: stages of cerebral haemodynamic impairment revisited. *Brain*, 125(3):595–607, March 2002.

[16] Manus J. Donahue, Jakob U. Blicher, Leif Ø stergaard, David A. Feinberg, Bradley J. MacIntosh, Karla L. Miller, Matthias Günther, and Peter Jezzard. Cerebral blood flow, blood volume, and oxygen metabolism dynamics in human visual and motor cortex as measured by whole-brain multi-modal magnetic resonance imaging. *Journal of cerebral blood flow and metabolism : official journal of the International Society of Cerebral Blood Flow and Metabolism*, 29(11):1856–66, November 2009.

[17] Manus J. Donahue, Hanzhang Lu, Craig K. Jones, Richard A. E. Edden, James J. Pekar, and Peter C. M. van Zijl. Theoretical and experimental investigation of the VASO contrast mechanism. *Magnetic resonance in medicine : official journal of the Society of Magnetic Resonance in Medicine / Society of Magnetic Resonance in Medicine*, 56(6):1261–73, December 2006.

[18] María a Fernández-Seara, Ze Wang, Jiongjiong Wang, Heng-Yi Rao, Matthias Guenther, David A. Feinberg, and John A. Detre. Continuous arterial spin labeling perfusion measurements using single shot 3D GRASE at 3 T. *Magnetic resonance in medicine : official journal of the Society of Magnetic Resonance in Medicine / Society of Magnetic Resonance in Medicine*, 54(5):1241–7, November 2005.

[19] Michael Frigge, D. C. Hoaglin, and Boris Iglewicz. Some implementations of the boxplot. *American Statistician*, 43(1):50–54, February 1989.

[20] K. J. Friston. Variational filtering. *NeuroImage*, 41(3):747–66, July 2008.

[21] K. J. Friston. Modalities, modes, and models in functional neuroimaging. *Science (New York, N.Y.)*, 326(5951):399–403, October 2009.

[22] K. J. Friston, A. Mechelli, R. Turner, and C. J. Price. Nonlinear responses in fMRI: the Balloon model, Volterra kernels, and other hemodynamics. *NeuroImage*, 12(4):466–77, October 2000.

[23] R. L. Grubb, M. E. Rarichle, J. O. Eichling, and M. M. Ter-Pogossian. The Effects of Changes in PaCO2 Cerebral Blood Volume, Blood Flow, and Vascular Mean Transit Time. *Stroke*, 5(5):630–639, September 1974.

[24] Hong Gu, Hanzhang Lu, Frank Q. Ye, Elliot A. Stein, and Yihong Yang. Noninvasive quantification of cerebral blood volume in humans during functional activation. *NeuroImage*, 30(2):377–87, April 2006.

[25] D. L. Hall and James Llinas. An introduction to multisensor data fusion. *Proceedings of the IEEE*, 85(1):6–23, 1997.

[26] Xiang He and Dmitriy A. Yablonskiy. Quantitative BOLD: mapping of human cerebral deoxygenated blood volume and oxygen extraction fraction: default state. *Magnetic resonance in medicine : official journal of the Society of Magnetic Resonance in Medicine / Society of Magnetic Resonance in Medicine*, 57(1):115–26, January 2007.

[27] David J. Heeger and David Ress. What does fMRI tell us about neuronal activity? *Nature reviews. Neuroscience*, 3(2):142–51, February 2002.

[28] Michael Hinze. Proper orthogonal decomposition surrogate models for nonlinear dynamical systems: Error estimates and suboptimal control. *Dimension Reduction of Large-Scale Systems*, 2005.

[29] Leigh A. Johnston, Eugene Duff, Iven Mareels, and Gary F. Egan. Nonlinear estimation of the BOLD signal. *NeuroImage*, 40(2):504–14, April 2008.

[30] R. E. Kalman. A New Approach to Linear Filtering and Prediction Problems. *Journal of Basic Engineering*, 82(1):35, 1960.

[31] R. Karlsson, T. Schon, and F. Gustafsson. Complexity analysis of the marginalized particle filter. *IEEE Transactions on Signal Processing*, 53(11):4408–4411, November 2005.

[32] Tariq Khan, Pradeep Ramuhalli, Donald O. Thompson, and Dale E. Chimenti. Particle Filter Based Multisensor Fusion for Solving Electromagnetic Nde Inverse Problems. *AIP Conference Proceedings*, 60(6):711–718, 2009.

[33] Stefan J. Kiebel, Jean Daunizeau, Christophe Phillips, and Karl J. Friston. Variational Bayesian inversion of the equivalent current dipole model in EEG/MEG. *NeuroImage*, 39(2):728–41, January 2008.

[34] K. K. Kwong. Dynamic Magnetic Resonance Imaging of Human Brain Activity During Primary Sensory Stimulation. *Proceedings of the National Academy of Sciences*, 89(12):5675–5679, June 1992.

[35] H. Laufs, A. Kleinschmidt, A. Beyerle, E. Eger, A. Salek-Haddadi, C. Preibisch, and K. Krakow. EEG-correlated fMRI of human alpha activity. *NeuroImage*, 19(4):1463–1476, August 2003.

[36] D. Lenzi, L. Serra, R. Perri, P. Pantano, G. L. Lenzi, E. Paulesu, C. Caltagirone, M. Bozzali, and E. Macaluso. Single domain amnestic MCI: a multiple cognitive domains fMRI investigation. *Neurobiology of aging*, 32(9):1542–57, September 2011.

[37] Terence S. Leung, Ilias Tachtsidis, Martin M. Tisdall, Caroline Pritchard, Martin Smith, and Clare E. Elwell. Estimating a modified Grubb's exponent in healthy human brains with near infrared spectroscopy and transcranial Doppler. *Physiological measurement*, 30(1):1–12, January 2009.

[38] P. Li, R. Goodall, and V. Kadirkamanathan. Estimation of parameters in a linear state space model using a Rao-Blackwellised particle filter. *IEE Proceedings - Control Theory and Applications*, 151(6):727, 2004.

[39] Chad Lieberman, Karen Willcox, and Omar Ghattas. Parameter and State Model Reduction for Large-Scale Statistical Inverse Problems. *SIAM Journal on Scientific Computing*, 32(5):2523, 2010.

[40] A. K. Liu, A. M. Dale, and J. W. Belliveau. Monte Carlo simulation studies of EEG and MEG localization accuracy. *Human Brain Mapping*, 16(1):47–62, May 2002.

[41] Nikos K. Logothetis. What we can do and what we cannot do with fMRI. *Nature*, 453(7197):869–78, June 2008.

[42] Nikos K. Logothetis and Brian A. Wandell. Interpreting the BOLD signal. *Annual review of physiology*, 66:735–69, January 2004.

[43] H. Lu, X. Golay, and J. J. Pekar. Sustained poststimulus elevation in cerebral oxygen utilization after vascular recovery. *J. Cereb. Blood Flow Metab.*, 24:764–770, 2004.

[44] Hanzhang Lu, Xavier Golay, James J. Pekar, and Peter C. M. Van Zijl. Functional magnetic resonance imaging based on changes in vascular space occupancy. *Magnetic resonance in medicine : official journal of the Society of Magnetic Resonance in Medicine / Society of Magnetic Resonance in Medicine*, 50(2):263–74, August 2003.

[45] R. C. Luo. Multisensor fusion and integration: approaches, applications, and future research directions. *IEEE Sensors Journal*, 2(2):107–119, April 2002.

[46] R. C. Luo, M. H. Lin, and R. S. Scherp. Dynamic multi-sensor data fusion system for intelligent robots. *Robotics and Automation, IEEE Journal of*, 4(4):386–396, 1988.

[47] R. Luypaert, S. Boujraf, S. Sourbron, and M. Osteaux. Diffusion and perfusion MRI: basic physics. *European Journal of Radiology*, 38(1):19–27, April 2001.

[48] J. B. Mandeville, J. J. Marota, C. Ayata, G. Zaharchuk, M. A. Moskowitz, B. R. Rosen, and R. M. Weisskoff. Evidence of a cerebrovascular postarteriole windkessel with delayed compliance. *Journal of cerebral blood flow and metabolism : official journal of the International Society of Cerebral Blood Flow and Metabolism*, 19(6):679–89, June 1999.

[49] Lawrence Murray and Amos Storkey. Continuous Time Particle Filtering for fMRI. pages 1–8.

[50] Frederic Mustiere, Miodrag Bolic, and Martin Bouchard. Rao-Blackwellised Particle Filters: Examples of Applications. In *2006 Canadian Conference on Electrical and Computer Engineering*, number 3, pages 1196–1200. IEEE, 2006.

[51] Tehrani Nik, Nejad Hossein, Seiichi Mita, and Han Long. Multi-Sensor Data Fusion for Autonomous Vehicle Navigation through Adaptive Particle Filter. In *Symposium A Quarterly Journal In Modern Foreign Literatures*, pages 752–759, 2010.

[52] Takayuki Obata, Thomas T. Liu, Karla L. Miller, Wen-Ming Luh, Eric C. Wong, Lawrence R. Frank, and Richard B. Buxton. Discrepancies between BOLD and flow dynamics in primary and supplementary motor areas: application of the balloon model to the interpretation of BOLD transients. *NeuroImage*, 21(1):144–153, January 2004.

[53] S. Ogawa. Brain Magnetic Resonance Imaging with Contrast Dependent on Blood Oxygenation. *Proceedings of the National Academy of Sciences*, 87(24):9868–9872, December 1990.

[54] P. Olesen. Combined analysis of DTI and fMRI data reveals a joint maturation of white and grey matter in a fronto-parietal network. *Cognitive Brain Research*, 18(1):48–57, December 2003.

[55] M. Plis, Sergey, D. Calhoun, Vince, P. Weisend, Michael, Tom Eichele, and Terran Lane. MEG and fMRI Fusion for Non-Linear Estimation of Neural and BOLD Signal Changes. *Frontiers in neuroinformatics*, 4(November):114, January 2010.

[56] C. Pohl and J. L. Van Genderen. Review article Multisensor image fusion in remote sensing: Concepts, methods and applications. *International Journal of Remote Sensing*, 19(5):823–854, January 1998.

[57] Bruce Rannala. Identifiability of parameters in MCMC Bayesian inference of phylogeny. *Systematic biology*, 51(5):754–60, October 2002.

[58] Jorge J. Riera, Jobu Watanabe, Iwata Kazuki, Miura Naoki, Eduardo Aubert, Tohru Ozaki, and Ryuta Kawashima. A state-space model of the hemodynamic approach: nonlinear filtering of BOLD signals. *NeuroImage*, 21(2):547–67, February 2004.

[59] Petra Ritter and Arno Villringer. Simultaneous EEG-fMRI. *Neuroscience and biobehavioral reviews*, 30(6):823–38, January 2006.

[60] T. Schon, F. Gustafsson, and P. J. Nordlund. Marginalized particle filters for mixed linear/nonlinear state-space models. *IEEE Transactions on Signal Processing*, 53(7):2279–2289, July 2005.

[61] A. Scouten and R. T. Constable. VASO-based calculations of CBV change: accounting for the dynamic CSF volume. *Magnetic resonance in medicine : official journal of the Society of Magnetic Resonance in Medicine / Society of Magnetic Resonance in Medicine*, 59(2):308–15, February 2008.

[62] Dahlia Sharon, Matti S. Hämäläinen, Roger B. H. Tootell, Eric Halgren, and John W. Belliveau. The advantage of combining MEG and EEG: comparison to fMRI in focally stimulated visual cortex. *NeuroImage*, 36(4):1225–35, July 2007.

[63] Wanyong Shin, Sandra W. Cashen, Ty A. Horowitz, Rahul Sawlani, and Timothy J. Carroll. Quantitative CBV measurement from static T1 changes in tissue and correction for intravascular water exchange. *Magnetic resonance in medicine : official journal of the Society of Magnetic Resonance in Medicine / Society of Magnetic Resonance in Medicine*, 56(1):138–45, July 2006.

[64] G. Simone and F. C. Morabito. NDT image fusion using eddy current and ultrasonic data. *COMPEL: The International Journal for Computation and Mathematics in Electrical and Electronic Engineering*, 20(3):857–868, 2001.

[65] Vaclav Smidl and Anthony Quinn. Accelerated Particle Filtering using the Variational Bayes Approximation. In *2007 IEEE International Conference on Acoustics, Speech and Signal Processing - ICASSP '07*, number 1, pages III–1173–III–1176. IEEE, April 2007.

[66] P. Staempfli, C. Reischauer, T. Jaermann, A. Valavanis, S. Kollias, and P. Boesiger. Combining fMRI and DTI: a framework for exploring the limits of fMRI-guided DTI fiber tracking and for verifying DTI-based fiber tractography results. *NeuroImage*, 39(1):119–26, January 2008.

[67] Chuili Sun and Juergen Hahn. Parameter reduction for stable dynamical systems based on Hankel singular values and sensitivity analysis. *Chemical Engineering Science*, 61(16):5393–5403, August 2006.

[68] Georgia Tsiliki and Sophia Kossida. Fusion methodologies for biomedical data. *Journal of proteomics*, pages 1–12, July 2011.

[69] Vasily A. Vakorin, Olga O. Krakovska, Ron Borowsky, and Gordon E. Sarty. Inferring neural activity from BOLD signals through nonlinear optimization. *NeuroImage*, 38(2):248–60, November 2007.

[70] Patrizia Vannini, Ove Almkvist, Thomas Dierks, Christoph Lehmann, and Lars-Olof Wahlund. Reduced neuronal efficacy in progressive mild cognitive impairment: a prospective fMRI study on visuospatial processing. *Psychiatry research*, 156(1):43–57, October 2007.

[71] Xiaohong Wan, Jorge Riera, Kazuki Iwata, Makoto Takahashi, Toshio Wakabayashi, and Ryuta Kawashima. The neural basis of the hemodynamic response nonlinearity in human primary visual cortex: Implications for neurovascular coupling mechanism. *NeuroImage*, 32(2):616–25, August 2006.

[72] G. Welch and Gary Bishop. An introduction to the Kalman filter. *Design*, 7(1):1–16, 2001.

[73] K. Willcox and J. Peraire. Balanced Model Reduction via the Proper Orthogonal Decomposition. *AIAA Journal*, 40(11):2323–2330, November 2002.

[74] Mark W. Woolrich, Peter Chiarelli, Daniel Gallichan, Joanna Perthen, and Thomas T. Liu. Bayesian inference of hemodynamic changes in functional arterial spin labeling data. *Magnetic resonance in medicine : official journal of the Society of Magnetic Resonance in Medicine / Society of Magnetic Resonance in Medicine*, 56(4):891–906, October 2006.

[75] Mark W. Woolrich, Saad Jbabdi, Brian Patenaude, Michael Chappell, Salima Makni, Timothy Behrens, Christian Beckmann, Mark Jenkinson, and Stephen M. Smith. Bayesian analysis of neuroimaging data in FSL. *NeuroImage*, 45(1 Suppl):S173–86, March 2009.

[76] Yi Wu, Edward Y. Chang, Kevin Chen-Chuan Chang, and John R. Smith. Optimal multimodal fusion for multimedia data analysis. In *Proceedings of the 12th annual ACM international conference on Multimedia - MULTIMEDIA '04*, page 572, New York, New York, USA, 2004. ACM Press.

[77] Martin Ystad, Erlend Hodneland, Steinunn Adolfsdottir, Judit Haász, Astri J. Lundervold, Tom Eichele, and Arvid Lundervold. Cortico-striatal connectivity and cognition in normal aging: a combined DTI and resting state fMRI study. *NeuroImage*, 55(1):24–31, March 2011.

[78] G. Zaharchuk, J. B. Mandeville, A. A. Bogdanov, R. Weissleder, B. R. Rosen, J. J. A. Marota, C. Iadecola, and S.-G. Kim. Cerebrovascular Dynamics of Autoregulation and Hypoperfusion: An MRI Study of CBF and Changes in Total and Microvascular Cerebral Blood Volume During Hemorrhagic Hypotension Editorial Comment: An MRI Study of CBF and Changes in Total and Microvascular Ce. *Stroke*, 30(10):2197–2205, October 1999.